ACS NANO

www.acsnano.org

ARTICLE

Multiplexed Graphene Quantum Dots with Excitation-Wavelength-Independent Photoluminescence, as Two-Photon Probes, and in Ultraviolet–Near Infrared Bioimaging

Wen-Shuo Kuo, Xing-Can Shen, Chia-Yuan Chang, Hui-Fang Kao, Sheng-Han Lin,* Jiu-Yao Wang,* and Ping-Ching Wu*

Cite This: *ACS Nano* 2020, 14, 11502–11509

Read Online

ACCESS | Metrics & More | Article Recommendations | Supporting Information

ABSTRACT: **In this study, sorted nitrogen-doped graphene quantum dots were prepared and subsequently conjugated with polymers. The synthesized materials exhibited excitation-wavelength-independent photoluminescence emissions ranging from ultraviolet to near-infrared and were 0.9−8.4 nm in size. The materials also exhibited high-photoluminescence quantum yields and excellent two-photon properties. Therefore, in two-photon bioimaging the materials with different emission spectra can be effective two-photon contrast agents. Specific antibodies were used to label organelles in cancer cells and identify nuclear antigens, thereby enabling the simultaneous detection of four targets in cells at a single two-photon excitation wavelength. The sorted nitrogen-doped graphene quantum dot materials were determined to be considerably more advantageous than organic dyes in identifying multiplexed targets, and they can be effective probes in cellular imaging.**

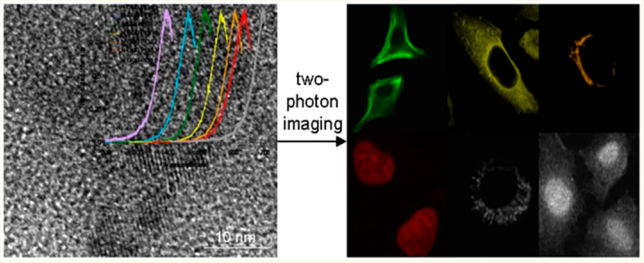

KEYWORDS: *size-based sorting graphene quantum dots, excitation-wavelength-independent photoluminescence, two-photon excitation, ultraviolet-near-infrared bioimaging, multiplexed targets*

Materials based on graphene quantum dots (GQDs) have been extensively researched and applied in drug delivery systems, DNA cleavage systems, sensors, photocatalysts, and energy-related applications; in particular, such materials are applied in bioimaging.[1,2] Doping is crucial for semiconductors because it enables clearly managing carrier density; this may thus result in entirely distinct optical and electrical properties compared with intrinsic properties.[3,4] Nitrogen (N) doping or nitrogen functionalization is effective for modifying the intrinsic properties of GQDs and carbon-based materials, including electronic, surface, and local chemical features.[5,6] Therefore, the band gap and chemical composition of GQDs can be modified and tuned, respectively, using N-GQDs with edge effects as well as quantum confinement; this likely enhances electrocatalytic, photochemical, and electrochemical activities, which are useful for realizing tunable luminescence in applications such as optoelectronics and bioimaging.[7−9] Accordingly, chemical doping is effective in modulating graphene's chemical, electronic, and optical properties.

Regarding optical properties, N-GQDs that are not sorted by size and have oxygen functionalities emit excitation-wavelength-dependent (EWD) photoluminescence (PL), which causes confusion regarding studied effects or restricts the use of N-GQDs as probes in relevant applications. Furthermore, elucidating quantum size effects is difficult because of defect states generated from such N-GQDs, which might contribute to EWD PL emissions.[10] Another primary factor contributing to emission phenomena is the inhomogeneous distribution of oxygenated sites.[11] Consequently, preparing oxygen (O)- and N-bearing GQDs might provide an opportunity and guide for understanding intrinsic and electronic properties related to optical behaviors associated with quantum-confined effects.

Received: May 11, 2020
Accepted: August 12, 2020
Published: August 12, 2020

Downloaded via UNIV OF LIVERPOOL on June 23, 2021 at 07:58:03 (UTC).
See https://pubs.acs.org/sharingguidelines for options on how to legitimately share published articles.

© 2020 American Chemical Society

https://dx.doi.org/10.1021/acsnano.0c03915
ACS Nano 2020, 14, 11502–11509

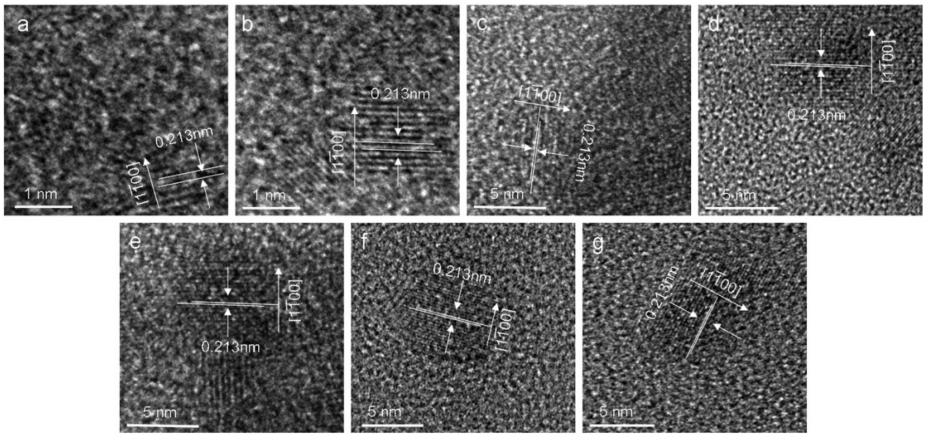

Figure 1. HRTEM images of (a) N-GQD0.9, (b) N-GQD1.7, (c) N-GQD3.8, (d) N-GQD5.9, (e) N-GQD6.8, (f) N-GQD7.4, and (g) N-GQD8.4 with diameters of 0.9 ± 0.1, 1.7 ± 0.1, 3.8 ± 0.2, 5.9 ± 0.2, 6.8 ± 0.3, 7.4 ± 0.2 nm, and 8.4 ± 0.3 nm, respectively. The images depict graphene {1$\bar{1}$00} lattice planes with a 0.213 nm *d*-spacing for the sorted N-GQDs.

A laser scanning microscope systematically coupled with a nonlinear multiphoton femtosecond laser can probe the optical properties of illuminated materials.[12] The wavelength range of such a microscope typically encompasses the near-infrared (NIR) region, which is a zone that affords low scattering, low energy absorption, minimal photobleaching, low tissue autofluorescence background levels, and maximal deep tissue penetration. Moreover, such a coupled laser has an enhanced detection limit because it enables noninvasive imaging of subcellular features and has a tissue penetration depth of less than 1 mm.

In the current study, graphene oxide sheets were subjected to an ultrasonic shearing reaction to prepare N-GQDs. The derived N-GQDs were sieved through polypropylene membranes to obtain sorted N-GQDs with homogeneous O and N distributions as well as high crystallinity and uniformity. These N-GQDs exhibited excitation-wavelength-independent (EWI)-PL emissions. Subsequently, the sorted N-GQDs were conjugated with a N atom-containing polymer (sorted N-GQD−polymer), resulting in a quantum confinement effect and the enhancement of the PL quantum yield (QY).[13] The sorted N-GQD−polymer had favorable two-photon properties, including strong two-photon absorption (TPA), a short lifetime, low two-photon luminescence (TPL) emission, absolute two-photon excitation (TPE) cross sections, a low ratio of radiative to nonradiative decay rates, and post-TPE stability; thus, the derived materials were determined to exhibit application potential as two-photon contrast agents that can facilitate exploration processes. This study used a nonlinear multiphoton femtosecond laser (also called a TPE laser) for excitation in the NIR region; the study also comprehensively analyzed the detection efficiency of the materials when used as probes by assigning specific labels [i.e., colors from ultraviolet (UV) to NIR regions] to various target at different subcellular levels and locations. Different organelles, marked using different colors, in a cell could be simultaneously and clearly identified by the sorted N-GQD−polymer conjugated with specific antibodies (N-GQD−polymer−Abs) for each organelle. Detection was achieved by performing excitation only once at an ultralow TPE power level of 14.7 nJ pixel^{-1} using 30 scans (excitation wavelength: 800 nm); see Supporting Information for calculation details. The *x*−*y*-axis focal point for the laser system was estimated to be 375.38 nm with the corresponding estimated *z*-axis resolution being 0.93 μm (Figure S1). Therefore, these results demonstrate the feasibility of the materials as contrast agents for two-photon imaging (TPI).

RESULTS AND DISCUSSION

Transmission electron microscopy (TEM) revealed that the mean lateral size of the derived N-GQDs was approximately 8.0 ± 0.6 nm (Figure S2a). Additionally, atomic force microscopy indicated that the thickness of a single layer of N-GQDs[14] was nearly 1.06 ± 0.05 nm (Figure S2b). Zeta potential spectroscopy revealed that the surface charge of the derived materials was approximately −18.2 mV, which was attributed to the presence of exposed carboxylic acid. Figures S2 and S3 illustrate the results obtained from other relevant characterization processes, confirming the successful preparation of N-GQDs. However, the as-prepared N-GQDs emitted EWD PL, which could be attributed to the quantum size effect, zigzag edge sites, and surface effect sites. Accordingly, size-based sorting was performed for the prepared N-GQDs. Specifically, the N-GQDs were sieved through polypropylene membranes of different pore sizes (i.e., 1, 5, 8, 10, 30, and 50 kDa). The sorted N-GQDs were then subjected to high-resolution TEM (HRTEM), yielding mean lateral sizes of 0.9 ± 0.1 nm (N-GQD0.9), 1.7 ± 0.1 nm (N-GQD1.7), 3.8 ± 0.2 nm (N-GQD3.8), 5.9 ± 0.2 nm (N-GQD5.9), 6.8 ± 0.3 nm (N-GQD6.8), 7.4 ± 0.2 nm (N-GQD7.4), and 8.4 ± 0.3 nm (N-GQD8.4) (Figure 1). The HRTEM results were consistent with those derived from Raman spectroscopy (Figure S4). Moreover, the calculated interlayer spacing in the materials was 0.213 nm (Figure 1), corresponding to the *d*-spacing of the {1$\bar{1}$00} graphene lattice plane. The entirety of the sorted N-GQDs measured approximately 1−2 nm in height, indicating one to two material layers (Figure S5). Furthermore, X-ray photoelectron spectroscopy was performed to analyze the sorted N-GQDs' surface chemistry. The N/C and O/C atomic ratios were 0.049−0.055 and 0.33−0.45, respectively, indicating that the sorted N-GQDs had similar degrees of surface oxidation (Figures S6−S8). As particle size increased, C—C/C═C was favorable for large materials. As N-GQD size decreased, the quantities of C—N, C—O, C═O, O—C═O, and pyridinic- or quaternary-N functionalities increased, and this was probably because of the increased edge sites,

https://dx.doi.org/10.1021/acsnano.0c03915
ACS Nano 2020, 14, 11502−11509

indicating that the quantity of O- and N-based groups influenced O and N content. However, the concentration of pyrrolic-N increased with N-GQD particle size probably because the oxidized interaction mainly occurred in five-membered aromatic heterocycles as N-GQD size increased. To probe the N-GQD surface functional groups, Fourier transform infrared spectroscopy was performed. Carboxyl, epoxy, and hydroxyl functional groups were exposed on the surface of the sorted N-GQDs (Figure S9). Additionally, zeta potential spectroscopy revealed that the surface charges of the sorted N-GQDs ranged from −16.3 to −17.5 mV (Table S1), which was attributed to the exposed carboxylic acid. The maximum and edge absorbances of the sorted N-GQDs were monitored using UV−visible (UV−vis) spectroscopy. Normalized maximal absorbance peaks occurred at approximately 225, 266, 314, 355, 378, 440, and 548 nm for N-GQD0.9, N-GQD1.7, N-GQD3.8, N-GQD5.9, N-GQD6.8, N-GQD7.4, and N-GQD8.4 respectively, and were attributed to the $\pi-\pi^*$ transition of aromatic C=C bonds (sp^2 domains), as presented in Figure S10. Moreover, edge absorbance peaks occurred at approximately 322, 384, 419, 467, 485, 546, and 610 nm for N-GQD0.9, N-GQD1.7, N-GQD3.8, N-GQD5.9, N-GQD6.8, N-GQD7.4, and N-GQD8.4, respectively, and were attributed to the n−π^* transition of the C=O shoulder and C—N. The maximal and edge absorbance peaks were related to the π-electron transition in the O- and N-containing GQDs. The PL spectra of the sorted N-GQDs exhibited a UV-to-NIR shift, as revealed by a PL spectrometer. Emission peaks determined for N-GQD0.9, N-GQD1.7, N-GQD3.8, N-GQD5.9, N-GQD6.8, N-GQD7.4, and N-GQD8.4 were noted at nearly 384, 450, 504, 549, 592, 626, and 690 nm, respectively, and exhibited the EWI-PL feature (Figure S11). Furthermore, the sorted N-GQDs exhibited different PL emissions in wavelengths encompassing the UV to NIR windows at 365 nm (Figure 2); these emissions were

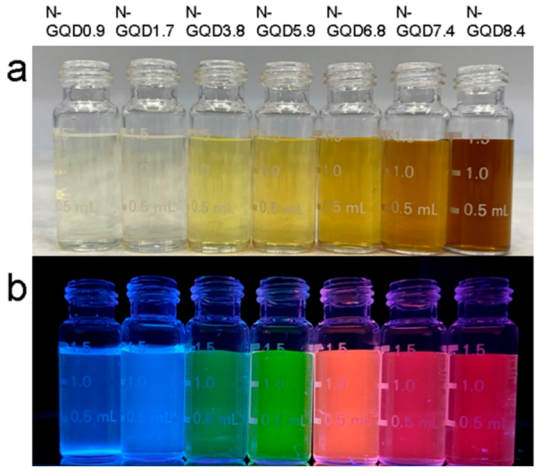

Figure 2. Photographs of sorted N-GQDs (a) without and (b) with 365 nm light excitation.

attributed to radiative π^*−n transitions.[11] Figure S12 presents the normalized PL excitation spectra, revealing the excitation wavelengths for local maximum PL emissions at peak wavelengths (Figure S11). Deconvolution revealed the following absorptive transition peaks: a long-wavelength peak attributed to the n → π^* transition, an intermediate-wavelength peak ascribed to the π → π^* transition, and a short-wavelength peak attributed to the n → σ^* transition. Furthermore, UV photoelectron spectroscopy was performed to determine the highest occupied orbital levels of the sorted N-GQDs. The n-state levels were located at nearly the same energetic positions (4.9−5.1 eV), regardless of size (Figure S13). Figure S14 illustrates the energy levels corresponding to the PL and absorption activities of the sorted N-GQDs. The quantum confinement effect due to particle size regulated the wavelengths of the radiative transitions. In addition, the sorted N-GQDs emitted EWI-PL, implying no trap states between the n-state and π^* energy levels. Changing the particle size did not cause disturbances in the n-state level; by contrast, as the considered particle size varied, the π, π^*, and σ^* orbital levels changed substantially. The EWI-PL of the sorted N-GQDs could be attributed to the π^* → n recombination that entailed an electron transition and phonon scattering. For short-wavelength-excitation-induced PL emissions, the electrons must relax from the σ^* to the π^* orbital. Furthermore, the relative QYs, measured with fluorescein dissolved in NaOH (0.1 M, pH 11) as the standard, of N-GQD0.9, N-GQD1.7, N-GQD3.8, N-GQD5.9, N-GQD6.8, N-GQD7.4, and N-GQD8.4 were 0.18, 0.21, 0.23, 0.26, 0.32, 0.34, and 0.38 respectively.[15] The characterization processes confirmed the successful preparation of sorted N-GQDs with EDI-PL characteristics.

Doping GQDs with N could efficiently increase their PL QYs. Analogously, the surface passivation or conjugation reactions of polymers, particularly those containing N, could yield high PL QYs because emissive energy trapped on a material surface is subjected to high quantum confinement.[13,16] In the present study, an amine group was present on polyethylenimine (PEI). Accordingly, the sorted N-GQDs' carboxyl groups and PEI formed the cross-linked PEI-N-GQD (N-GQD-PEI) materials.[17] Moreover, the sizes of the sorted N-GQD-PEI materials were estimated using Raman spectroscopy (for calculations, please see Supporting Information); the estimation revealed that the size of N-GQD-PEI1.1 (N-GQD0.9) was 1.1 nm, that of N-GQD-PEI2.0 (N-GQD1.7) was 2.0 nm, that of N-GQD-PEI4.2 (N-GQD3.8) was 4.2 nm, that of N-GQD-PEI6.3 (N-GQD5.9) was 6.3 nm, that of N-GQD-PEI7.1 (N-GQD6.8) was 7.1 nm, that of N-GQD-PEI7.7 (N-GQD7.4) was 7.7 nm, and that of N-GQD-PEI8.6 (N-GQD8.4) was 8.6 nm, indicating a slight increase in diameter (Figure S15). The surface charges of the sorted N-GQD-PEI materials became positive and ranged from 14.6 to 16.7 mV (Table S1) because of the exposed amine groups of PEI conjugated with the N-GQD surface, as confirmed by FTIR (Figure S16). Even after 3 months, the materials maintained favorable stability in a physiological environment (Table S2). Figure S17 presents the optical absorption spectra of the sorted N-GQD-PEI materials, demonstrating a characteristic PEI peak at approximately 208 nm and a red shift of the maximum absorbance wavelength, as compared to Figure S10. Furthermore, as illustrated in Figure S18, the EWI-PL spectra of the sorted N-GQD-PEI materials exhibited red-shift peaks at approximately 393 nm (N-GQD-PEI1.1), 462 nm (N-GQD-PEI2.0), 518 nm (N-GQD-PEI4.2), 560 nm (N-GQD-PEI6.3), 605 nm (N-GQD-PEI7.1), 636 nm (N-GQD-PEI7.7), and 698 nm (N-GQD-PEI8.6) compared with the data in Figure S11. Conjugating PEI with the sorted N-GQDs' surfaces increased the observed QYs for N-GQD-PEI1.1, N-GQD-PEI2.0, N-GQD-PEI4.2, N-GQD-PEI6.3, N-GQD-PEI7.1, N-GQD-PEI7.7, and N-GQD-PEI8.6 to 0.28, 0.30,

https://dx.doi.org/10.1021/acsnano.0c03915
ACS Nano 2020, 14, 11502−11509

Table 1. Sorted N-GQD-PEI Materials' Two-Photon Properties

	relative	absolute cross QY section of TPE (GM)	lifetime (ns)	radiative decay rate ($\times 10^8$ s^{-1})	nonradiative decay rate ($\times 10^8$ s^{-1})	ratio of radiative to nonradiative decay rates
N-GQD-PEI1.1	0.28	45512.8	1.47	1.90	4.90	0.39
N-GQD-PEI2.0	0.30	47107.5	1.32	2.27	5.30	0.43
N-GQD-PEI4.2	0.33	49588.6	1.21	2.73	5.54	0.49
N-GQD-PEI6.3	0.37	52330.8	1.15	2.88	4.91	0.59
N-GQD-PEI7.1	0.41	54702.8	1.11	3.69	5.32	0.69
N-GQD-PEI7.7	0.45	56980.3	1.01	4.46	5.45	0.82
N-GQD-PEI8.6	0.50	58372.2	0.95	5.26	5.26	1
Alexa Fluor 488	0.92[a]	372.5	1.17	7.86	0.68	11.56
Alexa Fluor 546	0.79[a]	309.2	1.14	6.93	1.84	3.77
Alexa Fluor 594	0.66[a]	251.6	1.12	5.89	3.04	1.94
Alexa Fluor 660	0.37[a]	174.3	1.10	3.36	5.73	0.59
Alexa Fluor 680	0.36[a]	138.0	0.93	3.87	6.88	0.56

[a]Information was available on the official Web site of Thermo Fisher Scientific, Waltham, MA, U.S.A.

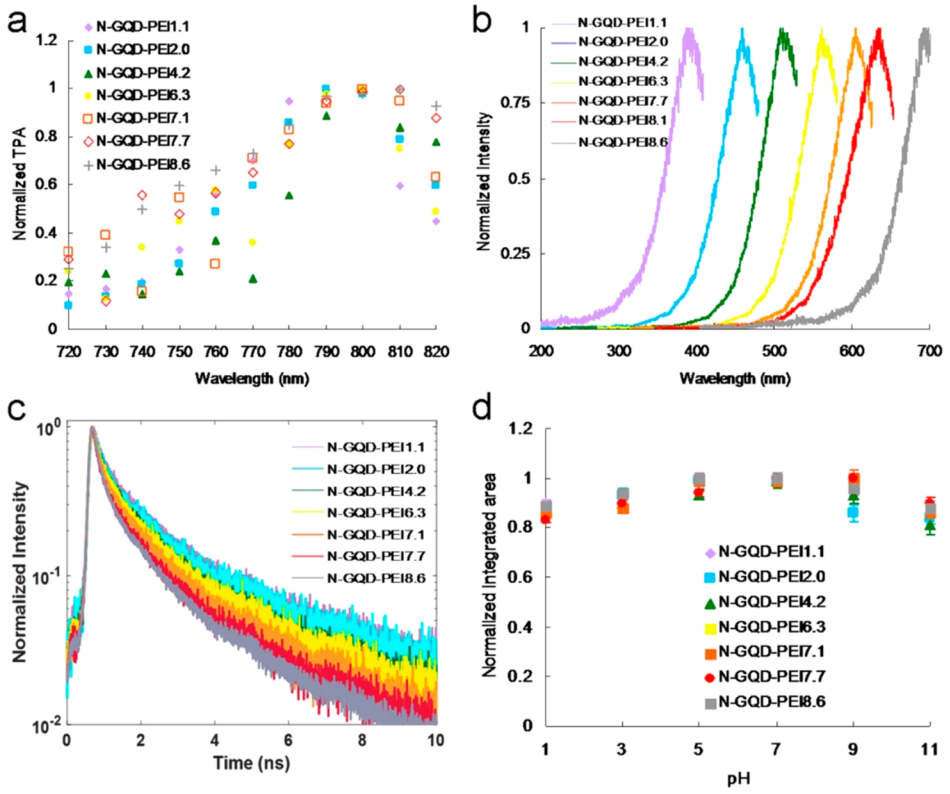

Figure 3. (a) Measured relative TPA spectra of the derived materials subjected to TPE at a set power of 70.4 nJ pixel^{-1} at 720−820 nm (n = 6). (b) Measured TPL spectra of the derived materials subjected to TPE at a set power of 105.6 nJ pixel^{-1}. A cutoff of 700 nm was determined through cascading filters (Ex: 800 nm). (c) Derived materials' time-resolved PL decay profile at room temperature (Ex: 800 nm). (d) TPL emission, as a pH function, of sorted N-GQD-PEI materials subjected to TPE at a set power of 105.6 nJ pixel^{-1} at 800 nm. As a pH (1−11) function, the TPL intensity of the integrated area was 350−700 nm, demonstrating the sorted N-GQD-PEI materials' high TPL intensity at the aforementioned pH values. Material dose delivered: 0.25 μg mL^{-1}. Data: mean ± SD (n = 6).

0.33, 0.37, 0.41, 0.45, and 0.50, respectively, relative to the standard reference (fluorescein in 0.1 M NaOH, pH 11),[15] as presented in Table 1. This occurred because size increased with diameter. On the basis of the enhanced emission effect caused by the cross-link, this study determined that PEI had potential fluorophores (tertiary as well as secondary amines), the derived N-GQDs had nonradiative structures and traps, and the observed PL enhancement was induced by rotation and vibration reduction related to the cross-linked PEI that was coated on the derived N-GQDs,[18] thereby increasing QY.

For the bioimaging study, a laser scanning microscope coupled with a nonlinear multiphoton femtosecond laser was prioritized because such a microscope can provide excitation wavelengths in the NIR region, a low average laser power that reduces the possibility of photodamage, and long-term deep observations. The relative maximum TPA ratio of the sorted N-GQD-PEI was first estimated to be 800 nm (Figure 3a); therefore, this ratio was used in subsequent experiments. When the most efficient excitation wavelength is applied, the derived materials could exhibit two-photon properties relevant to those of materials used in bioimaging and TPE. TPL is nonlinear

https://dx.doi.org/10.1021/acsnano.0c03915
ACS Nano 2020, 14, 11502−11509

with an intensity proportional to the square of the excitation power, QY, and TPE cross section. In this study, the sorted N-GQD-PEI materials were subjected to excitation and exhibited a two-photon phenomenon in which the observed TPL intensity depended on the excitation power quadratically with the corresponding exponents (logarithm) being 1.98–2.02 (Figure S19).[19] However, a large cross section is preferable when monitoring molecular actions. Accordingly, the large TPE cross sections of fluorophores render them useful for exploring two-photon techniques because the ratio of the absorbed energy to the input energy flux in biospecimens is high. In this study, for an applied TPE or one-photon excitation (OPE) resulting in the same QY,[12] the absolute TPE cross sections determined for the sorted N-GQD-PEI materials ranged approximately from 45512.8 to 58732.2 GM (Goeppert–Mayer units; 1 GM = 10^{-50} cm^4 s $photon^{-1}$); the cross sections were derived under TPE at 800 nm with Rhodamine B serving as the standard[20] (Tables 1 and 2 and Experimental Section in Supporting Information). Accordingly, the large cross sections derived for TPE and the increased QY indicate that a suitable TPL signal can be induced by enhanced localized excitation power and intrinsic fluorophores.[21] Figure 3b illustrates TPL spectra for the sorted N-GQD-PEI, indicating TPE-associated peaks at approximately 393 to 698 nm; this trend was similar to that for the emission wavelength derived using OPE (Figure S18). Additionally, a time-correlated single-photon counting technique was used to determine the lifetimes of the sorted N-GQD-PEI materials. This technique involved a triple exponential fitting function; that is, the average N-GQD-PEI1.1 lifetime was 1.47 ns, which was obtained by calculating the average of 0.17, 1.00, and 4.28 ns (Tables 1 and 3 and Figure 3c). Sequential radiative and nonradiative decay rates were 1.9×10^8 and 4.9×10^8 s^{-1}, respectively; the ratio of radiative to nonradiative decay rates was 0.39 (Table 1 and Experimental Section in Supporting Information). A reduced lifetime and increased QY could induce materials to primarily traverse the radiative pathway rather than the nonradiative pathway after TPE. The effectiveness of TPL radiative emission could be enhanced by doping GQDs with bonded N atoms; this is because sp^2 hybridization could be restored and delocalized electrons entering the π^* states could be donated, thereby increasing the absolute TPE cross section. Moreover, charge transfer efficiency could be enhanced by the large π-conjugated system as well as strong electron donation in the N-atom-containing polymers conjugated with N-GQDs. The N-GQD–polymer interaction also produced oscillating dipoles.[18] Additionally, as the sorted N-GQD–polymer materials' size increased, the PL QY and two-photon properties increased. Accordingly, evident increases or changes could be caused by the two-photon properties of the N-GQD–polymers, thus ensuring the efficacy of two-photon examinations.

Developing an efficient bioimaging approach necessitates laser scanning microscopy coupled with TPE as well as illuminated materials with high PL QYs and large cross sections. Moreover, specificity and accuracy can be enhanced by conjugating material surfaces with antibodies specific to organelles in accordance with manufacturer instructions (Conjugation Kit, Abcam, Cambridge, U.K.; Modification kit, Thermo Fisher Scientific, Waltham, MA, U.S.A.);[22,23] such antibodies include the antimicrotubule ($Ab_{microtubule}$), anti-

Table 2. TPE Cross Section of Materials at an Excitation Wavelength of 800 nm

reference	integrated emission intensity (counts)		action cross-section ($\eta\sigma$)
Rhodamine B[a]	291.6		158.3
analyte	integrated emission intensity (counts)	relative quantum yield (η)	absolute cross-section (σ)
N-GQD-PEI1.1	23474.6	0.28	45512.8
N-GQD-PEI2.0	26032.6	0.30	47107.5
N-GQD-PEI4.2	30144.1	0.33	49588.6
N-GQD-PEI6.3	35666.9	0.37	52330.8
N-GQD-PEI7.1	41314.3	0.41	54702.8
N-GQD-PEI7.7	47232.8	0.45	56980.3
N-GQD-PEI8.6	53762.9	0.50	58372.2
Alexa Fluor 488	630.6	0.92[b]	372.5
Alexa Fluor 546	450.3	0.79[b]	309.2
Alexa Fluor 594	305.9	0.66[b]	251.6
Alexa Fluor 660	118.8	0.37[b]	174.3
Alexa Fluor 680	91.5	0.36[b]	138.0

[a]Rhodamine B was selected as a reference to determine the TPE cross section. The relevant calculations are shown in Methods. [b]Information was available on the official Web site of Thermo Fisher Scientific, Waltham, MA, U.S.A.

Table 3. Lifetime Data and Parameters[a]

3 exp fitting model: (a0*exp(a1x)+a2*exp(a3x)+a4*exp(a5x)+a6)											
	a0	a1	a2	a3	a4	a5	a6	lifetime1	lifetme2	lifetime3	average lifetime (ns)
NGOD -PEI1.1	82.35	−5.99	154.82	−1.00	64.20	−0.23	1.48	0.17	1.00	4.28	1.47
N-GOD -PEI2.0	345.98	−4.63	508.18	−0.97	174.73	−0.23	1.01	0.22	1.03	4.33	1.32
N-GOD -PEI4.2	273.35	−5.10	433.82	−1.13	200.37	−0.30	7.79	0.20	0.88	3.29	1.21
N-GOD -PEI8.3	544.06	−6.10	694.48	−0.99	197.64	−0.23	−0.59	0.16	1.01	4.38	1.15
N-GOD -PEI7.1	258.76	−5.68	353.84	−1.08	120.39	−0.27	2.66	0.18	0.94	3.66	1.11
N-GOD -PEI7.7	611.97	−6.24	748.87	−1.10	245.95	−0.29	4.64	0.16	0.91	3.46	1.01
N-GOD -PEI8.8	381.95	−6.34	440.43	−1.12	127.97	−0.28	1.07	0.16	0.89	3.55	0.95
Alexa Flua 488	552.34	−5.58	718.70	−0.99	211.65	−0.23	−0.48	0.18	1.01	4.31	1.17
Alexa Fluor 546	475.91	−5.73	572.98	−0.97	157.90	−0.22	−1.61	0.17	1.03	4.46	1.14
Alexa Fluor 594	486.10	−5.90	557.84	−0.95	147.90	−0.22	−0.95	0.17	1.05	4.53	1.12
Alexa Fluor 660	617.80	−6.36	779.52	−1.03	235.26	−0.25	2.17	0.16	0.97	4.01	1.10
Alexa Fluor 680	2017.33	−5.96	2079.55	−1.08	532.36	−0.26	3.05	0.17	0.92	3.86	0.93

[a]Values and parameters generated using a time-correlated single-photon counting technique involving a triple-exponential fitting function for monitoring the emission at a wavelength of 800 nm under TPE.

https://dx.doi.org/10.1021/acsnano.0c03915
ACS Nano 2020, 14, 11502–11509

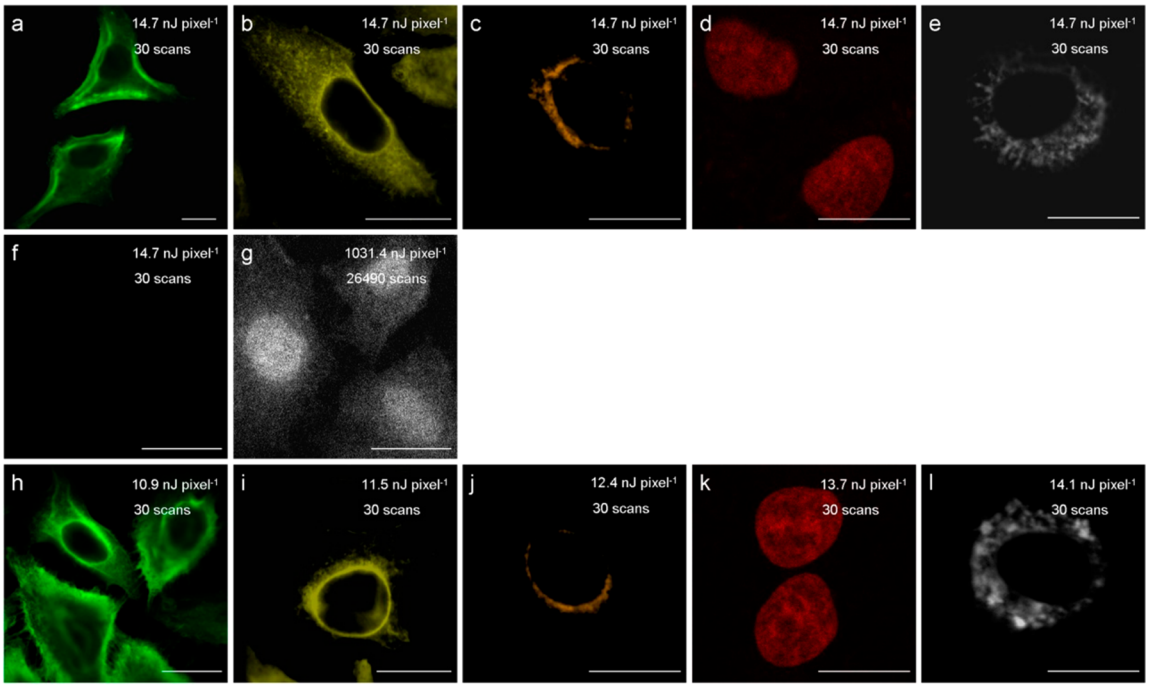

Figure 4. (a–e) TPL images captured in different N-GQD-PEI-Ab-treated A549 cells at a depth of 110 μm and TPE power of 14.7 nJ pixel^{-1} with 30 scans. (f) TPAF capture of untreated (i.e., unlabeled) cells at a depth of 110 μm and at the same TPE power or (g) a higher power of 1031.4 nJ pixel^{-1} with 26 490 scans. TPI for A549 cells treated at the same depth with (h) Ab$_{microtubule}$ (tubulin, YOL1/34)-Alexa Fluor 488, (i) Ab$_{mitochrodrion}$ (COX IV)-Alexa Fluor 546, (j) Ab$_{golgi}$ (GM130)-Alexa Fluor 594, (k) Ab$_{nucleus}$ (Lamin B1)-Alexa Fluor 660, and (l) Ab$_{ER}$ (KDEL)-Alexa Fluor 680 required power levels of 10.9, 11.5, 12.4, 13.7, and 14.1 nJ pixel^{-1} after 30 scans, respectively. Material dose delivered: 0.25 μg mL^{-1}. Excitation wavelength: 800 nm. Scale bar: 10 μm.

mitochondrial (Ab$_{mitochondrion}$), antigolgi (Ab$_{golgi}$), antinuclear (Ab$_{nucleus}$), and antiER (Ab$_{ER}$) antibodies. For the TPI investigation, malignant human lung carcinoma (A549) cells, which represent malignant human lung carcinoma, were used as the experimental template. Before the TPI investigation, the sorted N-GQD-PEI materials were subjected to necessary biocompatibility evaluations. The sorted N-GQD-PEI materials (i.e., N-GQD-PEI4.2, N-GQD-PEI6.3, N-GQD-PEI7.1, N-GQD-PEI7.7, and N-GQD-PEI8.6) had excellent biocompatibility (Figure S20), and they did not produce reactive oxygen species (ROS) in the cells. This study determined the absence of ROS by monitoring singlet oxygen ($^1O_2$) production by using a Singlet Oxygen Sensor Green reagent or trans-1-(2′-methoxyvinyl)pyrene and superoxide radical anion ($O_2^{\cdot-}$) with 2,3-bis (2-methoxy-4-nitro-5-sulfophenyl)-2H-tetrazolium-5-carboxanilide or glutathione (γ-L-glutamyl-L-cysteinyl-glycine, GSH)[12,14,17] (Tables S3–S7). Although GQD-based materials typically generate ROS after laser irradiation,[12,14] the absence of ROS in the N-GQD-PEI materials derived in the present study was probably because the conjugation of the polymer blocked ROS motility or activity. Furthermore, the sorted N-GQD-PEI materials exhibited high TPL emission intensity in the acidic or weak basic environments of cancerous specimens or tissues. Therefore, the materials have the potential for use as two-photon contrast probes (Figure 3d). N-GQD-PEI-Ab-treated A549 cells were subjected to TPI at different depths in cells embedded in a collagen matrix[12] to imitate three-dimensional (3D) epithelial tissues. The TPL emission originating from the sorted A549 cells treated with N-GQD-Ab was also examined under a single TPE executed at 14.7 nJ pixel^{-1} (with 30 scans) at an imaging depth of 110 μm. Figure 4 displays the TPI results. The emission wavelength was 800 nm (Figure 4a–e), yielding clear images of the cells and organelle locations because of the successful conjugation of different antibodies. When N-GQD-PEI4.2-Ab$_{microtubule}$, N-GQD-PEI6.3-Ab$_{mitochrondrion}$, N-GQD-PEI7.1-Ab$_{golgi}$, N-GQD-PEI7.7-Ab$_{nucleus}$, and N-GQD-PEI8.6-Ab$_{ER}$ were used, the corresponding organelles had green, yellow, orange, red, and NIR emissions, respectively, which were consistent with the TPL wavelengths in Figure 3b. Additionally, for intrinsic fluorophores of cells that were not treated with the synthesized materials (i.e., unlabeled cells), detecting the emitted two-photon autofluorescence (TPAF) at the same depth and TPE energy remained difficult (Figure 4f) unless a higher energy level of approximately 1031.4 nJ pixel^{-1} with 26 490 scans was used (Figure 4g); therefore, the TPI results could not have been confounded. Additionally, TPI execution was not negatively affected by spherical aberrations caused by the immersion oil–TPE sample mismatch in terms of refractive index even at a depth of 110 μm.

The sorted N-GQD-PEI materials for TPI exhibited stability. As the scan time increased to 66 225, the TPI results remained visible and clear (Figures S21a–e); moreover, a 3 month observation demonstrated that the sorted N-GQDs-PEI materials subjected to TPE for 6 min (approximately 79 470 scans) at 800 nm exhibited nearly no decrease in TPL intensity (Figure S22). Therefore, the materials had high photostability that was maintained even after 3 months. Moreover, because materials subjected to TPE are flexible, the TPI and fluorescence change of conventional commercial fluorophores could be observed through *in vitro* experiments. Accordingly, Ab$_{microtubule}$ (tubulin, YOL1/34)-Alexa Fluor 488, Ab$_{mitochrodrion}$ (COX IV)-Alexa Fluor 546, Ab$_{golgi}$ (GM130)-Alexa Fluor 594, Ab$_{nucleus}$ (Lamin B1)-Alexa Fluor 660, and Ab$_{ER}$(KDEL)-Alexa

https://dx.doi.org/10.1021/acsnano.0c03915
ACS Nano 2020, 14, 11502–11509

Fluor 680 were selected in the current study because of their favorable photoproperties.[24] Compared with the sorted N-GQD-PEI materials, the Alexa Fluor dyes could be detected in TPI (Figure 4h–l) at lower power levels to maintain TPL intensity, as illustrated in Figure 4a–e, because of their high QYs, high ratios of radiative to nonradiative decay rates (Table 1), and short lifetimes (Table 3). However, as the scan time increased to 66 225 at a TPE power of 14.7 nJ pixel^{-1}, the TPI revealed intensity decay (Figure S21f–j), and the Alexa Fluor dyes exhibited an increased photobleaching effect after 6 min of exposure (approximately 79 470 scans; Figure S23). Regardless of the applied target, the corresponding intensities of the emitted fluorescence of the sorted N-GQD-PEI materials were robust to photobleaching, whereas those of the Alexa Fluor dyes were vulnerable to photobleaching. These results indicate that the sorted N-GQD-PEI materials possess greater photostability than widely used conventional fluorophores (i.e., Alexa Fluor dye series); thus, the synthesized materials in this study provide suitable alternatives for biological applications.

CONCLUSIONS

Systematically coupling a laser scanning microscope with a nonlinear multiphoton femtosecond laser provides a promising imaging approach with high subcellular and spatial resolution as well as excellent sensitivity that could reach the single-molecule level. Most cellular functions involve collaboration among numerous proteins, necessitating techniques for simultaneously probing multiple biological targets in a cell. This necessity has motivated innovation in fluorescent labels that enable the multiplexed labeling of targets in cells. The present study synthesized sorted N-GQD–polymer materials with EWI-PL emission characteristics. The synthesized materials had excellent photoproperties when subjected to TPE; therefore, they can be used as effective two-photon contrast agents in TPI. In addition, the prepared materials had narrow emission ranges, and there was size-dependent effect of two-photon properties. Consequently, the materials can be used with multiple colors from UV to NIR regions without spectral overlap. In particular, all suggested colors can be excited simultaneously through TPE by applying a single wavelength. These exceptionally bright, highly photostable, and multiplexing-compatible sorted N-GQD–polymer materials are suitable for use as fluorescence probes in biological and biomedical applications for analyzing multiplexed targets.

METHODS

Femtosecond Laser Optical System for Fluorescence Lifetime Imaging Microscopy (FLIM). Key components of our instrument/microscope include a femtosecond, Ti-sapphire laser (Tsunami, Spectra-Physics, Santa Clara, CA, U.S.A.) with a pulse width of less than 100 fs and a repetition rate of 80 MHz, an inverted optical microscope (Axiovert 200, Zeiss, Oberkochen, Germany), an x–y galvanometer scanner (6215H, Cambridge, MA, U.S.A.), a triple-axis sample-positioning stage (ProScanII, Prior Scientific Instruments Ltd., Cambridge, U.K.), a z-axis piezoelectric nanopositioning stage (Nano-F100, Mad City Laboratories, Madison, WI, U.S.A.), an acousto-optic modulator (Neos, 23080-x-1.06-LTD, BMI Surplus Inc., Hanover, MA, U.S.A.), photomultiplier tubes (H5783P, Hamamatsu, Shizuoka Prefecture, Japan), and a data acquisition card with an field-programmable gate array module (PCI-7831R, National Instruments, Austin, TX, U.S.A.). A detailed description of the multiphoton fabrication instrument can be found in previous studies. For FLIM, the time-correlated single photon counting (TCSPC) module (PicoHarp 300, PicoQuant, Berlin, Germany) is integrated into the main control platform based on LabVIEW programming, which triggers the synchronic signal through the FPGA module, collects the fluorescence time-to-digital data through a USB 2.0 interface, and then constructs the fluorescence lifetime image by using LabVIEW. The time-to-digital data from different pixels are separated by inserting a marker signal from scanning the synchronic trigger. To facilitate the 3D lifetime image and data analysis, the LabVIEW program also records the scanning parameters corresponding to the time-to-digital data. The timer overflow signal of the TCSPC module is removed, allowing the accumulated time-to-digital data of each pixel to form a histogram. Nonlinear least-squares algorithm is used to fit the fluorescence lifetime decay curve for each pixel. In accordance with the fitting lifetime data of each pixel and the pixel scanning information, the FLIM image can be displayed with a resolution of 0.05 ns under the main control platform. The lifetime data and the parameter were generated using the triple-exponential equation fitting while monitoring the emission under TPE (Ex: 800 nm).

TPI. A549 cells (5×10^3) per well in a 96-well culture plate were incubated overnight in the dark at 37 °C with 5% CO_2 in air. All of the sorted N-GQD-PEI-antibody (Ab) or the Alexa-Ab were added to the incubated cells to process the interaction of antibody–antigen for 2.5 h of incubation in the dark at 37 °C. Next, the medium was removed and replaced with the new culture medium; this was repeated 3–5 times to wash out the nonspecific binding. The cells were embedded in a collagen matrix to mimic the three-dimensional epithelium tissue. The TPI of the sorted N-GQD-PEI-Ab or the Alexa-Ab were observed using a nonlinear femtosecond laser microscopy optical system under TPE.

There is no batch-to-batch variation for the materials in terms of two-photon properties and two-photon contrast agents. A different optical system has different detection depth. Because of the detection efficiency and the objective we used, the maximal z-depth we can observe by this laser optical system is approximately 120 μm. However, 110 μm in the work can show the optimal resolution in the mimic 3D biological specimens.

Complete materials and methods for this article can be found in the Supporting Information.

ASSOCIATED CONTENT

Supporting Information

The Supporting Information is available free of charge at https://pubs.acs.org/doi/10.1021/acsnano.0c03915.

Methods; z-axis resolution of laser system; characterizations; photoluminescence excitation and UPS spectra; energy level diagram; stability of materials in physiological environment; TPL intensity dependence on the excitation power; TPE cross section; MTT assay; measurements of ROS; TPI; photostability (PDF)

AUTHOR INFORMATION

Corresponding Authors

Sheng-Han Lin – *Department of Anesthesiology, E-Da Hospital, Kaohsiung 824, Taiwan, Republic of China*; Email: ed111667@edah.org.tw

Jiu-Yao Wang – *Allergy and Clinical Immunology Research Center, National Cheng Kung University Hospital, College of Medicine and Department of Pediatrics, National Cheng Kung University Hospital, College of Medicine, National Cheng Kung University, Tainan 701, Taiwan, Republic of China*; Email: a122@mail.ncku.edu.tw

Ping-Ching Wu – *Department of Biomedical Engineering, National Cheng Kung University, Tainan 701, Taiwan, Republic of China*; Email: wbcxyz@bme.ncku.edu.tw

https://dx.doi.org/10.1021/acsnano.0c03915
ACS Nano 2020, 14, 11502–11509

Authors

Wen-Shuo Kuo − *School of Chemistry and Materials Science, Nanjing University of Information Science and Technology, Nanjing 210044, Jiangsu, China; Allergy and Clinical Immunology Research Center, National Cheng Kung University Hospital, College of Medicine, National Cheng Kung University, Tainan 701, Taiwan, Republic of China;* orcid.org/0000-0002-2364-2482

Xing-Can Shen − *State Key Laboratory for the Chemistry and Molecular Engineering of Medicinal Resources (Ministry of Education), School of Chemistry and Pharmaceutical Sciences, Guangxi Normal University, Guilin 541004, China;* orcid.org/0000-0002-7116-6919

Chia-Yuan Chang − *Department of Mechanical Engineering, National Cheng Kung University, Tainan 701, Taiwan, Republic of China*

Hui-Fang Kao − *Department of Nursing, National Tainan Junior College of Nursing, Tainan 700, Taiwan, Republic of China*

Complete contact information is available at: https://pubs.acs.org/10.1021/acsnano.0c03915

Notes

The authors declare no competing financial interest.

ACKNOWLEDGMENTS

This work was supported by Research Start-Up Fund of Nanjing University of Information Science & Technology, China (2018r047), National Natural Science Foundation of China, China (21977022 and 21671046), E-Da Hospital, Taiwan, Republic of China, and Ministry of Science and Technology, Taiwan, Republic of China (MOST 108-2314-B-006-053-).

REFERENCES

(1) Gong, K.; Du, F.; Xia, Z.; Durstock, M.; Dai, L. Nitrogen-Doped Carbon Nanotube Arrays with High Electrocatalytic Activity for Oxygen Reduction. *Science* **2009**, *323*, 760−764.

(2) Peng, J.; Gao, W.; Gupta, B. K.; Liu, Z.; Romero-Aburto, R.; Ge, L.; Song, L.; Alemany, L. B.; Zhan, Z.; Gao, G.; Vithayathil, S. A.; Kaipparettu, B. A.; Marti, A. A.; Hayashi, T.; Zhu, J. J.; Ajayan, P. M. Graphene Quantum Dots Derived from Carbon Fibers. *Nano Lett.* **2012**, *12*, 844−849.

(3) Tian, P.; Tang, L.; Teng, K. S.; Lau, S. P. Graphene Quantum Dots from Chemistry to Applications. *Mater. Today Chem.* **2018**, *10*, 221−258.

(4) Palaniselvam, T.; Valappil, M. O.; Illathvalappil, R.; Kurungot, S. Nanoporous Graphene by Quantum Dots Removal from Graphene and Its Conversion to a Potential Oxygen Reduction Electrocatalyst *via* Nitrogen Doping. *Energy Environ. Sci.* **2014**, *7*, 1059−1067.

(5) Son, D. I.; Kwon, B. K.; Park, D. H.; Seo, W. S.; Yi, Y.; Angadi, B.; Lee, C. L.; Choi, W. K. Emissive ZnO-Graphene Quantum Dots for White-Light-Emitting Diodes. *Nat. Nanotechnol.* **2012**, *7*, 465−417.

(6) Tetsuka, H.; Asahi, R.; Nagoya, A.; Okamoto, K.; Tajima, I.; Ohta, R.; Okamoto, A. Optically Tunable Amino-Functionalized Graphene Quantum Dots. *Adv. Mater.* **2012**, *24*, 5333−5338.

(7) Santiago, S. R. M.; Wong, Y. A.; Lin, T. N.; Chang, C. H.; Yuan, C. T.; Shen, J. L. Effect of Nitrogen Doping on the Photoluminescence Intensity of Graphene Quantum Dots. *Opt. Lett.* **2017**, *42*, 3642−3645.

(8) Li, Y.; Zhao, Y.; Cheng, H.; Hu, Y.; Shi, G.; Dai, L.; Qu, L. Nitrogen-Doped Graphene Quantum Dots with Oxygen-Rich Functional Groups. *J. Am. Chem. Soc.* **2012**, *134*, 15−18.

(9) Wang, X.; Li, X.; Zhang, L.; Yoon, Y.; Weber, P. K.; Wang, H.; Guo, J.; Dai, H. N-Doping of Graphene through Electrothermal Reactions with Ammonia. *Science* **2009**, *324*, 768−771.

(10) Tang, L.; Ji, R.; Cao, X.; Lin, J.; Jiang, H.; Li, X.; Teng, K. S.; Luk, C. M.; Zeng, S.; Hao, J.; Lau, S. P. Deep Ultraviolet Photoluminescence of Water-Soluble Self-Passivated Graphene Quantum Dots. *ACS Nano* **2012**, *6*, 5102−5110.

(11) Wang, L.; Wang, H. Y.; Wang, Y.; Zhu, S. J.; Zhang, Y. L.; Zhang, J. H.; Chen, Q. D.; Han, W.; Xu, H. L.; Yang, B.; Sun, H. B. Direct Observation of Quantum-Confi ned Graphene-Like States and Novel Hybrid States in Graphene Oxide by Transient Spectroscopy. *Adv. Mater.* **2013**, *25*, 6539−6545.

(12) Kuo, W. S.; Shao, Y. T.; Huang, K. S.; Chou, T. M.; Yang, C. H. Antimicrobial Amino-Functionalied Nitrogen-Doped Graphene Quantum Dots for Eliminating Multidrug-Resistant Species in Dual-Modality Photodynamic Therapy and Bioimaging under Two-Photon Excitation. *ACS Appl. Mater. Interfaces* **2018**, *10*, 14438−14446.

(13) Sun, Y. P.; Zhou, B.; Lin, Y.; Wang, W.; Fernando, K. A. S.; Pathak, P.; Meziani, M. J.; Harruff, B. A.; Wang, X.; Wang, H.; Luo, P. G.; Yang, H.; Kose, M. E.; Chen, B.; Veca, L. M.; Xie, S. Y. Quantum-Sized Carbon Dots for Bright and Colorful Photoluminescence. *J. Am. Chem. Soc.* **2006**, *128*, 7756−7757.

(14) Kuo, W. S.; Chen, H. H.; Chen, S. Y.; Chang, C. Y.; Chen, P. C.; Hou, Y. I.; Shao, Y. T.; Kao, H. F.; Hsu, C. L. L.; Chen, Y. C.; Chen, S. J.; Wu, S. R.; Wang, J. W. Graphene Quantum Dots with Nitrogen-Doped Content Dependence for Highly Efficient Dual-Modality Photodynamic Antimicrobial Therapy and Bioimaging. *Biomaterials* **2017**, *120*, 185−194.

(15) Togashi, D. M.; Szczupak, B.; Ryder, A. G.; Calvet, A.; O'Loughlin, M. Investigating Tryptophan Quenching of Fluorescein Fluorescence under Protolytic Equilibrium. *J. Phys. Chem. A* **2009**, *113*, 2757−2767.

(16) Xu, Q.; Liu, Y.; Gao, C.; Wei, J.; Zhou, H.; Chen, Y.; Dong, C.; Sreeprasad, T. S.; Li, N.; Xia, Z. Synthesis, Mechanistic, Investigation, and Application of Photoluminescence Sulfur and Nitrogen Co-Doped Carbon Dots. *J. Mater. Chem. C* **2015**, *3*, 9885−9893.

(17) Kuo, W. S.; Chang, C. N.; Chang, Y. T.; Yeh, C. S. Amtimicrobial Gold Nanorods with Dual-Modality Photodynamict Inactivation and Hyperthermia. *Chem. Commun.* **2009**, 4853−4855.

(18) Zhu, S.; Wang, L.; Zhou, N.; Zhao, X.; Song, Y.; Maharjan, S.; Zhang, J.; Lu, L.; Wang, H.; Yang, B. The Corsslink Enhanced Emission (CEE) in Non-Conjugated Polymer Dots: From the Photoluminescence Mechanism to the Cellular Uptake Mechanism and Internalization. *Chem. Commun.* **2014**, *50*, 13845−13848.

(19) Horton, N. G.; Wang, K.; Kobat, D.; Clark, C. G.; Wise, F. W.; Schaffer, C. B.; Xu, C. *In Vivo* Three-Photon Microscopy of Subcortical Structures within an Intact Mouse Brain. *Nat. Photonics* **2013**, *7*, 205−209.

(20) Xu, C.; Webb, W. W. Measurement of Two-Photon Excitation Cross Sections of Molecular Fluorophores with Data from 690 to 1050 nm. *J. Opt. Soc. Am. B* **1996**, *13*, 481−491.

(21) Li, B.; Wu, C.; Wang, M.; Charan, K.; Xu, C. An Adaptive Excitation Source for High-Speed Multiphoton Microscopy. *Nat. Methods* **2020**, *17*, 163−166.

(22) Rizvi, A. H.; Camara, P. G.; Kandror, E. K.; Roberts, T. J.; Schieren, I.; Maniatis, T.; Rabadan, R. Single-Cell Topological RNA-Seq Analysis Reveals Insights into Cellular Differentiation and Development. *Nat. Biotechnol.* **2017**, *35*, 551−560.

(23) Ning, X.; Guo, J.; Wolfert, M. A.; Boons, G. J. Visualizing Metabolically Labeled Glycoconjugates of Living Cells by Copper-Free and Fast Huisgen Cycloadditions. *Agnew. Chem. Int. Ed.* **2008**, *47*, 2253−2255.

(24) Panchuk-Voloshina, N.; Haugland, R. P.; Bishop-Stewart, J.; Bhalgat, M. K.; Millard, P. J.; Mao, F.; Leung, W. Y.; Hauland, R. P. Alexa Dyes, a Series of New Fluorescent Dyes that Yield Exceptionally Bright, Photostable Conjugates. *J. Histochem. Cytochem.* **1999**, *47*, 1179−1188.

Supporting Information

Multiplexed Graphene Quantum Dots with Excitation-Wavelength-Independent Photoluminescence, as Two-Photon Probes, and in Ultraviolet-Near Infrared Bioimaging

Wen-Shuo Kuo,[†,‡] Xing-Can Shen,[§] Chia-Yuan Chang,[$] Hui-Fang Kao,[#] Sheng-Han Lin,[%] Jiu-Yao Wang,*[‡,⊥] and Ping-Ching Wu*[&]*

[†]School of Chemistry and Materials Science, Nanjing University of Information Science and Technology, Nanjing 210044, Jiangsu, China

[‡]Allergy & Clinical Immunology Research Center, National Cheng Kung University Hospital, College of Medicine, National Cheng Kung University, Tainan 701, Taiwan (R.O.C.)

[§]State Key Laboratory for the Chemistry and Molecular Engineering of Medicinal Resources (Ministry of Education), School of Chemistry and Pharmaceutical Sciences, Guangxi Normal University, Guilin 541004, China

[$]Department of Mechanical Engineering, National Cheng Kung University, Tainan 701, Taiwan (R.O.C.)

[#]Department of Nursing, National Tainan Junior College of Nursing, Tainan 700, Taiwan (R.O.C.)

[%]Department of Anesthesiology, E-Da Hospital, Kaohsiung 824, Taiwan (R.O.C.)

[⊥]Department of Pediatrics, National Cheng Kung University Hospital, College of Medicine, National Cheng Kung University, Tainan 701, Taiwan (R.O.C.)

[&]Department of Biomedical Engineering, National Cheng Kung University, Tainan 701, Taiwan (R.O.C.)

*Correspondence: ed111667@edah.org.tw (S.H. Lin); a122@mail.ncku.edu.tw (J.Y. Wang); wbcxyz@bme.ncku.edu.tw (P. C. Wu)

METHODS

Preparation of nitrogen doped graphene quantum dots (N-GQDs) and sorted N-GQDs.[1] Graphene oxide was prepared from a natural graphite powder (Bay carbon Inc., Bay City, MI, USA) using a modified Hummers' method. Graphite (8.5 M) and $NaNO_3$ (0.6 M) (Merck & Co., Kenilworth, NJ, USA) were mixed with H_2SO_4 (Sigma Aldrich Co., St Louis, MO, USA). $KMnO_4$ (2.0 M) (FUJIFILM Wako Chemicals USA Inc., Richmond, VA, USA) was slowly added with continual stirring at 35 °C overnight. Subsequently, ddH_2O was gradually added and continually stirred. H_2O_2 (Sigma Aldrich Co., St Louis, MO, USA) was added to terminate the reaction. Washing and centrifugation with ddH_2O were performed several times, and the graphene oxide was collected. The as-prepared graphene oxide was placed in a tube furnace and heated to 400–600 °C in the presence of ammonia for 4–6 h; it was subsequently introduced to concentrated HNO_3 (16.0 M) (Sigma Aldrich Co., St Louis, MO, USA) and stirred for 2 days. The mixture was placed in a sonicator for 2 days and subsequently placed in an oven at 160 °C for 1 day to vaporize all the liquid. Washing and centrifugation (83000 rpm; Optima TLX Ultracentrifuge, Optima TLX Ultracentrifuge, Beckman Coulter Inc., Danville, CA, USA) with ddH_2O were conducted several times. The supernatant was filtered through a 0.22 μm microporous membrane. The pH of the resulting black suspension was tuned to 7.4 with NaOH (Sigma Aldrich Co., St Louis, MO, USA), and N-GQDs were obtained.

The N-GODs were sieved using centrifugation tubes equipped with polypropylene membranes filters with cut-off molecular weights of 1, 5, 8, 10, 30, and 50 kD (Satorius, Göttingen, Germany) to obtain the sorted N-GQDs. The N-GOD suspension was flowed through membranes arranged in a sequence of decreasing pore size and collected at serial stages to form the sorted N-GQDs of varying sizes.

Characterization. Materials were subject to transmission electron microscope (TEM, JEOL 2100F and JEOL 3010, Akishima, Tokyo, Japan) observation. The height profile diagram, thickness and size of samples were determined by atomic force microscopy (AFM, multimode 8, Bruker, Billerica, MA, USA). The crystalline structures of samples were identified using X-ray diffraction (XRD, AXS Gmbh, Billerica, MA, USA). Fourier transform infrared (FTIR), ultraviolet-visible (UV-vis), and zeta potential spectra of samples were recorded by the spectrometers: PerkinElmer RX1 (PerkinElmer, Waltham, MA, USA), U-4100 Hitachi (Chiyoda-ku, Tokyo, Japan) and Manern Nano-ZS90 (Worcestershire, West Midlands, UK), respectively. Raman spectroscopy (DXR, Thermo Scientific, Waltham, MA, USA) was used to examine the crystallinity of samples with 532 nm laser. X-ray photoelectron spectroscopy (XPS) (PHI 5000, VersaProbe, Chanhassen, MN, USA) was employed to examine the surface chemistry of the materials, the O(1s)/C(1s) and N(1s)/C(1s) atomic ratios of materials. The Photoluminescence (PL) signal was recorded by the spectrophotometer (F-7000, Hitachi, Chiyoda-ku, Tokyo, Japan).

The sorted-N-GQDs conjugated with polymer material (sorted-N-GQD-polymer). Positively charged polyethylenimine (PEI) (20 μg mL^{-1}; Sigma Aldrich Co., St Louis, MO, USA) were mixed with 1-ethyl-3-(3-dimethylaminopropyl) carbodiimide (EDC), a crosslinker reagent (20 μg mL^{-1}; Sigma Aldrich Co., St Louis, MO, USA), and then added the sorted-N-GQDs (5 μg mL^{-1}) to establish covalent bonds between the sorted N-GQDs' carboxyl groups and PEI to form N-GQD-polymer materials. The solutions were centrifuged (82000 rpm; Optima TLX Ultracentrifuge, Optima TLX Ultracentrifuge, Beckman Coulter

Inc., Danville, CA, USA) for 20 min to remove excess polymers. The pellets (N-GQD-polymer materials) were resuspended in ddH_2O, and the centrifugation process was repeated several times. The sorted-N-GQD-PEI materials were obtained.

Antibody (Ab) conjugation.[2,3] The absorbance of a certain quantity of Ab (abcam, Cambridge, UK) was recorded *via* UV-vis spectroscopy (Absorbance: approximately 276 nm). According to the manufacturer's instructions (Conjugation Kit, UK; Modification kit, Thermo Fisher Scientific, Waltham, MA, USA), the materials were reacted with the same quantity antibody overnight in the dark (4 ℃) and then centrifuged (83000 rpm) to remove excess Ab; the material-Ab was then then prepared. Conversely, the supernatant was retained and its absorbance measured. The difference between the absorbance of the collected supernatant and the original antibody was estimated. Consequentially, the quantity of the Ab conjugated on the materials was calculated by Lambert-Beer's law. In the working solution of 1×PBS buffer, approximately 18.5 μg of $Ab_{microtubule}$ conjugated on 100 μg of N-GQD-PEI4.2. This implies that the conjugation efficiency of 1×PBS buffer was approximately 18.5%, and it was 17.8%, 18.0%, 19.2% and 19.4% for N-GQD-PEI6.3-$Ab_{mitochondrion}$, N-GQD-PEI7.1-$Ab_{golgi,}$ N-GQD-PEI7.7-$Ab_{nucleus,}$ and N-GQD-PEI8.6-$Ab_{ER,}$ respectively. Additionally, for $Ab_{EGFR\ (epidermal\ growth\ factor\ receptor)}$, N-GQD-PEI4.2, N-GQD-PEI6.3, N-GQD-PEI7.1 and N-GQD-PEI7.7, and N-GQD-PEI8.6 was 18.2%, 18.6%, 18.5%, 18.3%, and 18.7% respectively. The above results had also proven the successful conjugation of Ab on the surface of materials.

Cell culture and Cytotoxicity (MTT) assay.[4,5] The malignant human lung carcinoma (A549) cells were cultured in Dulbecco's modification Eagle's medium (DMEM) (Thermo Fisher Scientific, Waltham, MA, USA) + 10% Fetal Bovine Serum (Thermo Fisher Scientific, Waltham, MA, USA) at 37℃ under 5% CO_2 in air. The cells were collected by trypsinization and placed onto a 10 cm tissue culture Petri dish, then allowed to grow for 2-4 days. For cytotoxicity assay, cells (5×10^3 per well in a 96-well culture plate) were incubated overnight and then treated with the sorted N-GQD-PEI-Ab (delivered dose: 0.25–1.0 μg mL^{-1}) for 24 h incubation in an incubator (37 ℃). The culture medium was removed and replaced with the new culture medium containing. Repeat for 3 to 5 times to wash out the nonspecific binding. MTT reagents (10%) (Sigma Aldrich Co., St Louis, MO, USA) followed by incubation for 4 h at 37 ℃, leading to the formation of formazan dye. The medium was then changed with dimethyl sulfoxide (DMSO, 200 μL) (Fisher Scientific, Hampton, NH, USA) for 10 min, followed by centrifugation at 4000 rpm for 10 min. The supernatant was transferred into a new ELISA plate and the absorbance was measured at A540 with an ELISA reader (Thermo Electron, Waltham, MA, USA). Data are means ± SD (n = 6).

Quantum yield (QY) measurement.[6,7] The relative PL QY of contrast agent is usually the ratio of the emitted photons to the absorbed photons and is given as follows:

$$QY = QY_{ref}\,(\eta^2/\eta_{ref}^2)(I/A)(A_{ref}/I_{ref}) \qquad \text{(Equation S1)}$$

, where $QY_{ref} = 0.28$ is the QY of fluorescein/ 0.1M NaOH (pH11; Sigma Aldrich Co., St Louis, MO, USA) as a reference, η is the refractive index of ddH_2O=1.333, I is the integrated fluorescence intensity and A is the absorbance at the excitation wavelength. One-photon excitation or two-photon excitation (TPE) yields the same QY. The relative QYs of the sorted N-GQDs were approximately 0.18 (N-GQD0.9), 0.21 (N-GQD1.7), 0.23 (N-GQD3.8), 0.26 (N-GQD5.9), 0.32 (N-GQD6.8), 0.34 (N-GQD7.4), and 0.38

(N-GQD8.4) respectively. By the conjugation with PEI on the surfaces of the sorted N-GQDs, the QYs were increased to 0.28, 0.30, 0.33, 0.37, 0.41, 0.45, and 0.50, respectively, for the sizes increased with the diameters.

Femtosecond laser optical system for the measurements of two-photon absorption (TPA) and two-photon luminescence (TPL).[8,9] The Ti-sapphire (ti-sa) femtosecond laser (Tsunami, Spectra-Physics, Santa Clara, CA, USA) optical system with a pulse width of less than 100 fs and a repetition rate of 80 MHz, an inverted optical microscope (Axiovert 200, Zeiss, Oberkochen, Germany), a *x*-*y* galvanometer scanner (6215H, Cambridge, MA, USA), a triple-axis sample-positioning stage (ProScan^{TM}II, Prior Scientific Instruments Ltd., Cambridge, UK), a *z*-axis piezoelectric nano-positioning stage (Nano-F100, Mad City Labs, Madison, WI, USA), an acousto-optic modulator (AOM) (Neos 23080-x-1.06-LTD, BMI Surplus Inc., Hanover, MA, USA), photomultiplier tubes (PMTs) (H5783P, Hamamatsu, Shizuoka Prefecture, Japan), and a data acquisition (DAQ) card with a field-programmable gate array (FPGA) module (PCI-7831R, National Instruments, Austin, TX, USA). ***TPA measurement.*** A femtosecond laser with a wavelength range of 720–820 nm and was used to excite TPA signals. A time-average luminescence photon count (F) is proportional to the cross section (δ) of TPA and can be given as

$$F \approx \frac{1}{2}\delta\eta_2\phi C\frac{g_p}{f\tau}\frac{8nP^2}{\pi\lambda}, \qquad \text{(Equation S2)}$$

where C the concentration of the photoinitiator, η_2 is the quantum efficiency of photoluminescence, ϕ the luminescence collection efficiency of the system, P the average incident power, g_p the dimensionless quantity for degree of the second-order temporal coherence, f the pulse repetition rate, n the refractive index of the measurement medium, λ the excitation wavelength and τ the excitation pulse width by full-width at half maximum. After the SF-10 prism pair compensation, the parameters which are the collection system, the pulse repetition rate, the concentration of the materials and the excitation power can be maintained the same at different excitation wavelengths with their corresponding excitation pulse widths. On the basis of the measured excitation pulse width, the measured fluorescence photon count and the excitation wavelength, the TPA was derived as $\delta \times \eta_2$. *Via* the SPC module, the PMTs were used to collect the PL photon The TPA can be given as

$$\delta\eta_2 \propto \lambda\tau F. \qquad \text{(Equation S3)}$$

An in-lab constructed autocorrelator was used to monitor the pulse widths of the different wavelengths after the objective. With a galvanometer scanner speed of 2 m ms^{-1}, the excitation spectrum was measured as 720-820 nm with an excitation power of 2.0 mW [this is the power before objective; the power after objective (or on sample) is 0.704 mW (or 70.4 nJ pixel^{-1})]. Therefore, the relative TPA spectrum as function of excitation wavelength for the material was measured. ***Measurement of TPL spectrum.*** The material was exposed to TPE from the femtosecond laser at an excitation wavelength of 800 nm, a power of 105.6 nJ pixel^{-1} (1.056 mW), a scanning area of 200 μm × 200 μm, a frequency of 10 kHz, an exposure time of 1.638 s/(scan, pixel)= 100 μs, 128 × 128 pixels scan^{-1}, and a pixel area of 1562.5 nm × 1562.5 nm. The focal spot

area was calculated as $\pi d^2/4$, where d = 0.61 λ/numerical aperture (*NA*) is the full width at half maximum of the beam waist. For instance, at the *x*–*y* axis focal spot with 800 nm excitation and a 40× oil-immersion objective with an *NA* of 1.3, d = 0.61 × 800 nm/1.3 = 375.38 nm, and the *z*-axis resolution was measured to be 0.93 μm (**Figure S1**). For 800 nm excitation, the exposure time per scan for an individual nanomaterial is expressed as (focal spot area/pixel area) × 100 = 4.53 ms, and the total exposure time t = 4.53 ms × number of scans. A 40× oil-immersion objective (*NA* 1.3) was used to collect the signals, and the detection range of the spectrum photometer was 300-700 nm.

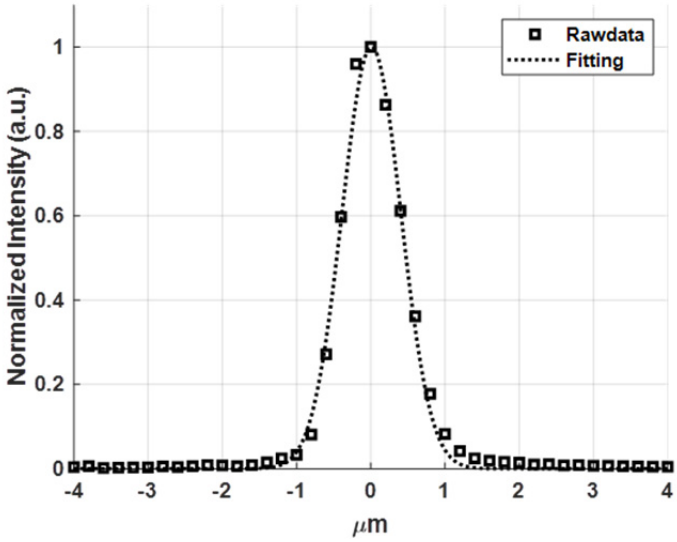

Figure S1. According to the *z* axis scan of a gold thin film to measure the signal of second harmonic generation at different position, the *z* axis resolution of the laser system (full width at half maximum) is around 0.93 μm (fitting using Gaussian function).

Additionally, the calculations of laser power (mW or J pixel^{-1}) used on the sample were as follows. For the 40× oil-immersion objective (*NA* 1.3), the transmission rate at 800nm in wavelength is approximately 88% in this optical system, and the laser power went from the output to the objective with only 40% of the original output power due to the loss of power. As a result, the calculated energy after the objective (on sample) is P_{output}(mW)*40%*88%= 0.352*P_{output} (mW). For instance, P_{output} = 3.0 mW, the calculated energy after the objective (on the sample) is 3.0 mW*40%*88%= 1.056 mW. With 10 kHz of scan rate (each pulse stays 0.1 ms pixel^{-1}), the calculated energy on the sample (J pixel^{-1}) was around P_{output} (mW)*40%*88%*0.1 ms= 0.0352*P_{output} (J pixel^{-1}). For instance, P_{output} = 3.0 mW, the energy (J pixel^{-1}) on sample= 3.0 mW*40%*88%*0.1 ms= 0.1056 μJ pixel^{-1}= 105.6 nJ pixel^{-1}. The power after the objective (on the sample) was used and marked throughput this manuscript.

Measurement of TPE absolute cross section.[8-13] The absolute cross section of TPE was measured on the basis of luminescence signals by using a femtosecond laser optical system, as described by previous studies. A 40× oil-immersion objective (*NA* 1.3) was overfilled by expansion of the laser beams. For the multiphoton excitation, the diffraction-limited illumination of the sample was approximately achieved and analyzed. Under TPE and for the thick sample limit, the relation between time-averaged luminescence

photon flux $\langle F^{(n)}(t) \rangle$ and the incident power $P(t)$ can be obtained. The formula can be given as

$$\langle F^{(n)}(t) \rangle = \frac{1}{n} \frac{g_p^{(n)}}{(f\tau)^{n-1}} \phi \eta \sigma_n C n_0 \frac{a_n (\mathrm{NA})^{2n-4} \langle P(t) \rangle^n}{8\pi^{3-n} \lambda^{2n-3}}$$

(Equation S4)

, where C is the concentration of the fluorophore, n is the number of photons absorbed (n = 2 for the TPE), ϕ is the system collection efficiency, τ is the laser pulse width, f is the laser repetition rate, η is the luminescence quantum efficiency (or quantum yield), and λ is the excitation wavelength in vacuum, σ_n is the n-photon excitation cross section, and a_2 = 64 for TPE. $g_p^{(n)}$ is the n^{th}-order temporal coherence of the excitation source. Due to the limitation of resource we currently have, $\langle F^{(n)}(t) \rangle$ is temporarily not able to be calculated and the values could be replaced by the integrated TPL intensity with the symbol "counts". As a result, the equation for action cross section ($\eta\sigma_2$) is turned into

$$\eta\sigma_2 = \frac{\text{counts}}{\frac{1}{2} \frac{g_p^{(2)}}{f_\tau} n_0 \phi C \frac{8\langle P(t) \rangle^2}{\pi\lambda}}$$

(Equation S5)

If it was with the same 2nd-order temporal coherence of the excitation source, the laser pulse width, laser repetition rate, incident power, system collection efficiency, wavelength and working concentration, the action cross section of TPE ($\eta\sigma_2$) for a fluorophore as the reference compound is determined relative to the known action cross section, then the Equation S5 is simplified as

$$(\eta\sigma_2)_2 = \frac{\text{counts}_2}{\text{counts}_1} (\eta\sigma_2)_1$$

(Equation S6)

, where Sample 1 means the reference compound, and sample 2 means the fluorophore.

TPL of fluorescein and rhodamine B (Sigma-Aldrich, St. Louis, MO, USA) needed to be verified. After measuring the dependence of the emission intensity on the excitation power range of 704 nJ pixel^{-1} (7.04 mW) to 2816 nJ pixel^{-1} (28.16 mW) (Ex: 800 nm) (**Figure S19**). According to the previous studies, the action cross section of TPE for fluorescein and rhodamine B is 36.4 and 153.0 Göeppert–Mayer units (GM; 1 GM = 10^{-50} cm^{4}s photon^{-1}), respectively, for 800 nm excitation. We also referred to the free website http://www.drbio.cornell.edu/cross_sections.html, kindly provided by Prof. Chris Xu (Cornell University, NY, USA). Based on Equation S5, the TPE action cross section of fluorescein and rhodamine B were calculated to be 37.5 and 158.3 GM, respectively (**Table S8**), which indicated an error of less than 5% compared with those from Prof. Xu's laboratory. In this study, rhodamine B was chosen as the standard reference for determining the cross section, and the calculated absolute cross sections of TPE for the sorted N-GQD-PEI were from approximately 45512.8 GM to 58372.2 GM (**Table 2**), respectively. The measured parameters for calculating the TPE absolute cross section of sorted-N-GQD-PEI is shown in **Table 1**. No batch to batch variation was observed for the materials in two-photo properties, and two-photon contrast agents.

Femtosecond laser optical system for fluorescence lifetime imaging microscopy (FLIM).[8,9] Key components of our instrument/microscope include a femtosecond, ti-sa laser (Tsunami, Spectra-Physics, USA) with a pulse width of less than 100 fs and a repetition rate of 80 MHz, an inverted optical microscope (Axiovert 200, Zeiss, Germany), a *x*-*y* galvanometer scanner (6215H, Cambridge, USA), a triple-axis sample-positioning stage (ProScan^{TM}II, Prior, UK), a *z*-axis piezoelectric nano-positioning stage (Nano-F100, Mad City Labs, USA), an AOM (23080-x-1.06-LTD, Neos, USA), PMTs (H5783P, Hamamatsu, Japan), and a DAQ card with an FPGA module (PCI-7831R, National Instruments, USA). A detailed description of the multiphoton fabrication instrument can be found in previous studies. For FLIM, the time-correlated single photon counting (TCSPC) module (PicoHarp 300, PicoQuant) is integrated into the main control platform based on LabVIEW programming, which triggers the synchronic signal through the FPGA module, collects the fluorescence time-to-digital data through a USB 2.0 interface, and then constructs the fluorescence lifetime image by using LabVIEW. The time-to-digital data from different pixels is separated by inserting a marker signal from scanning the synchronic trigger. To facilitate three-dimensional (3D) lifetime image and data analysis, the LabVIEW program also records the scanning parameters corresponding to the time-to-digital data. The timer overflow signal of the TCSPC module is removed, allowing the accumulated time-to-digital data of each pixel to form a histogram. Nonlinear least square algorithm is used to fit the fluorescence lifetime decay curve for each pixel. In accordance with the fitting lifetime data of each pixel and the pixel scanning information, the FLIM image can be displayed with a resolution of 0.05 ns under the main control platform. The lifetime data and the parameter generated using the triple-exponential equation fitting while monitoring the emission under TPE (Ex: 800 nm) (**Table 3**). Additionally, the average lifetime is estimated by the lifetimes with different weighting individually.

$$t_{average} = \frac{1}{a_0 + a_1 + a_4}(a_0 \cdot t_1 + a_2 \cdot t_2 + a_3 \cdot t_3) \quad \text{(Equation S7)}$$

$t_{average}$: average lifetime, t_1:lifetime, t_2:lifetime2, t_3:lifetime3

Calculation of radiative and non-radiative decay rates.[14,15] PL QY and lifetime are both major parameters when investigating the emission characteristics of fluorescent dyes in diverse environments. The quantum yield Q can be expressed as follows:

$$Q = \frac{\Gamma}{\Gamma + k} \quad \text{(Equation S8)}$$

, where Γ is the radiative decay rate and k is the non-radiative decay rate.

Fluorescence lifetime is usually defined as the average time required for an electron in the excited state to decay to the ground state. The TPL lifetime τ can also be relative to the decay rates and is described as follows:

$$\tau = \frac{1}{\Gamma + k} \quad \text{(Equation S9)}$$

Following Equations (S8-S9), the radiative and non-radiative decay rates can be calculated.

Upon the absorption of a photon, one of the weakly bound electrons of the fluorescent molecule—a fluorophore—is promoted to a higher energy level. The fluorophore is then said to be in an excited state, A^*.

This state is metastable, and therefore the fluorophore will return to its stable ground state, *A*. It can do so either radiatively by emitting a fluorescence photon *hv*,

$A^* \rightarrow A + hv$

or nonradiatively, for example, by dissipating the excited state energy as heat

$A^* \rightarrow A$ + heat

The depopulation of the excited state depends on the de-excitation pathways available. Fluorescence is the radiative deactivation of the lowest vibrational energy level of the first electronically excited singlet state, S_1, back to the electronic ground state, S_0. The singlet states are the energy levels that can be populated by the weakly bound electron without a spin flip. The absorption and emission processes are illustrated by an energy level diagram named after Aleksander Jablonski.

The fluorescence lifetime, τ, is the average time a fluorophore remains in the electronically excited state S_1 after excitation. τ is defined as the inverse of the sum of the rate parameters for all excited state depopulation processes: Equation S7, where the nonradiative rate constant k is the sum of the rate constant for internal conversion, k_{ic}, and the rate constant for intersystem crossing to the triplet state, k_{isc}, so that $k = k_{ic},+ k_{isc}$. The fluorescence emission always occurs from the lowest vibrational level of S_1, a rule known as Kasha's rule, indicating that the fluorophore has no memory of its excitation pathway, *e.g.* OPE and TPE yield the same fluorescence spectrum, QY and lifetime.

Reactive oxygen species (ROS) detection.[4,5,16-24] ***Singlet oxygen ($^1O_2$).*** (a) Material-Ab (0.25 μg mL^{-1}) was treated with A549 cells, after which it was subjected to 3 h of incubation at 37 °C in darkness. Subsequently, the mixture was exposed to TPE photoexcitation [14.7 nJ $pixel^{-1}$ for 6 min (approximately 79470 scans); Ex: 800 nm] and finally mixed with Singlet Oxygen Sensor Green (SOSG) reagent (1 μM; Thermo Fisher Scientific, Waltham, MA, USA) (Ex/Em: 488/525 nm). A fluorescence spectrometer was employed for measurements. For ROS neutralization, the mixture was mixed with 30 ppm of antioxidant *α*-tocopherol/methyl linoleate (Sigma-Aldrich, St. Louis, MO, USA) in darkness and exposed to TPE photoexcitation with the same treatment. (b) Material-Ab (0.25 μg mL^{-1}) was treated with A549 cells, after which it was subjected to 3 h of incubation at 37 °C in darkness. Subsequently, the mixture was exposed to TPE photoexcitation [14.7 nJ $pixel^{-1}$ for 6 min (approximately 79470 scans); Ex: 800 nm] and finally mixed with 10 μM of trans-1-(2′-methoxyvinyl)pyrene (*t*-MVP) (Thermo Fisher Scientific, Waltham, MA, USA)/0.10 M SDS (Sigma-Aldrich, St. Louis, MO, USA) (Ex/Em: 352/465 nm). For ROS neutralization, the mixture was mixed with 30 ppm of antioxidant *α*-Tocopherol/methyl linoleate (Sigma-Aldrich, St. Louis, MO, USA) in darkness. Reaction of *t*-MVP with $^1O_2$ yields a dioxetane intermediate that fluoresces while it decomposes into 1-pyrenecarboxaldehyde. Furthermore, this highly selective fluorescent probe does not react with other activated oxygen species such as hydroxyl radicals, superoxide, or hydrogen peroxide. A fluorescence spectrometer was employed for measurements. ROS neutralization was conducted with the

same as previously described treatment. ***Superoxide radical anion ($O_2^{\cdot-}$).*** (a) Material-Ab (0.25 μg mL^{-1}) was treated with A549 cells, after which it was subjected to 3 h of incubation at 37 °C in darkness. Subsequently, the mixture was exposed to TPE photoexcitation [14.7 nJ $pixel^{-1}$ for 6 min (approximately 79470 scans); Ex: 800 nm] and finally mixed with 2,3-bis (2-methoxy-4-nitro-5-sulfophenyl)-2H-tetrazolium-5-carboxanilide (XTT) (0.45 mM; Sigma-Aldrich, St. Louis, MO, USA). The purpose of this material was that it interacted with $O_2^{\cdot-}$ and produced XTT-formazan, resulting in strong absorption (470 nm in wavelength). A UV-vis spectrometer was employed to monitor this absorption. For ROS neutralization, the mixture was mixed with 30 ppm of antioxidant *α*-tocopherol/methyl linoleate (Sigma-Aldrich, St. Louis, MO, USA) in darkness and exposed to TPE photoexcitation with the same treatment. (b) Material-Ab (0.25 μg mL^{-1}) was treated with A549 cells, after which it was subjected to 3 h of incubation at 37 °C in darkness. Subsequently, the mixture was exposed to TPE photoexcitation [14.7 nJ $pixel^{-1}$ for 6 min (approximately 79470 scans); Ex: 800 nm] and finally mixed with 50 mM bicarbonate buffer (pH 8.60) and glutathione (*γ*-L-glutamyl-L-cysteinyl-glycine, GSH) (Sigma-Aldrich, St. Louis, MO, USA)/0.80 mM bicarbonate buffer (the Ellman's assay for $O_2^{\cdot-}$ detection). Subsequently, the following experiments were conducted according to the procedure in a previous study. Loss of GSH (%) was calculated as the difference in absorbance between the sample and negative control divided by the absorbance of the negative control. The signal of the generated $O_2^{\cdot-}$ was obtained as described in the previous calculation. Data are presented as mean ± SD (n = 6).

Two-photon imaging (TPI). 5×10^3 A549 cells per well in a 96-well culture plate were for overnight of incubation in the dark at 37°C with 5% CO_2 in air. All of the sorted N-GQD-PEI-Ab or the Alexa488-Ab were respectively added to the incubated cells to process the interaction of antibody-antigen for 2.5 h of incubation in the dark at 37°C. Remove and replace with the new culture medium and repeat for 3 to 5 times to wash out the nonspecific binding. The cells wee embedded in a collagen matrix to mimic the three-dimensional epithelium tissue. And the TPI of the sorted N-GQD-PEI-Ab or the Alexa488-Ab were observed using a nonlinear femtosecond laser microscopy optical system under TPE.

And there is no batch to batch variation for the materials in terms of two-photo properties, and two-photon contrast agents. Different optical system has different detection depth. Due to the detection efficiency and the objective we used, the maximal z depth we can be observed by this laser optical system is around 120 μm. However, 110 μm in the work can show the optimal resolution in the mimic 3D biological specimens.

N-GQDs, the estimated mean lateral size of the derived N-GQDs was 8.0 ± 0.6 nm prepared by an ultrasonic shearing reaction from graphene oxide sheets (**Figure S2a**). The diagram of height profile was determined by AFM, showing the image of a 1.06 ± 0.05 nm thick single layer of N-GQDs (**Figure S2b**). The typical thickness of a GQD with about a 0.4-0.7 nm increase in graphene thickness (~0.36 nm) was known due to the existence of hydroxyl, carboxyl and epoxy groups on two sides of the oxide surface. For the UV-vis absorption spectrum of the N-GQDs, the peaks can be observed. The N-GQDs showed peaks about 226 nm ($\pi-\pi^*$ transition of aromatic C=C bonds), and 324 nm ($n-\pi^*$ transition of C=O shoulder and C−N) (**Figure S2c**). FTIR was used to analyze the exposed functional groups of N-GQD (**Figure S2d**). Results showed characteristic bands of N-GQDs for epoxy stretching about 1033 cm^{-1} (band 1), C−O stretching about 1109 cm^{-1} (band 2), phenolic C−OH stretching about 1210 cm^{-1} (band 3), tertiary alcoholic C−OH bending about 1362 cm^{-1} (band 4), symmetric carboxylate $C(=O)_2^-$, sp^2 C=N and sp^3 C−N stretching about 1416, 1425 and 1440 cm^{-1} (band 5), C=C ring stretching about 1637 cm^{-1} (band 6), C=O stretching 1755 cm^{-1} (band 7), carboxylate O−H and N−H in-plane stretching 3228 and 3379 cm^{-1} (band 8). The results indicated the functional groups of carboxyl, hydroxyl and epoxy were exposed from N-GQDs. Raman spectroscopy was also used to examine the crystallinity of N-GQDs (**Figure S2e**). The major feature bands of N-GQDs are the so-called G bands (~1609 cm^{-1}), which result from the in-plane vibration in a two-dimensional hexagonal lattice of sp^2 hybridized C-C bonds; the D band resulted from the defect, disorder, and sp^3-hybridized carbon in graphene layers by breaking the translational symmetry of the lattice occurring at about 1382 cm^{-1}. The results showed that the integrated intensity ratio of the D and G bands (I_D/I_G ratio), which represents the extent of disorder, was 0.84, which is much higher than that of graphite (0.105), clearly indicating higher distortion of the N-GQDs. Besides, the initial graphene film has a I_D/I_G of 1.1, which was reduced to 0.84 after the oxidation reaction.[25] This result indirectly indicates that the defect lies within the graphene film having been preferentially attacked for the oxidation to break the starting reduced graphene oxide film into tiny pieces of fewer defects, hence the observed reduced I_D/I_G, indicating the successful conversion from graphite, graphene oxide to N-GQDs. XRD, which was performed to analyze crystallinity, showed the diffraction angle of the small size of N-GQDs peaked broadly at about 24.41°, which means an interlayer distance of 0.358 nm (**Figure S2f**). The XRD results suggested that there was no significant basal plane functionalization, which is consistent with our understanding that the graphenes have the much more active edges than the in-plane carbons, as well as the existence of functional groups at the edges of the N-GQDs. The value for one N-GQD is in agreement with values, 0.340–0.403 nm, reported for the N-GQD prepared with other methods and the as-prepared N-GQDs were confirmed to have a lamellar, well-ordered structure. The accommodation of various oxygen species, such as carboxyl, hydroxyl and epoxy groups, and changes in the carbon hexahedron grid plane that increase the spacing of the graphene layers result in the increased basal spacing of the N-GQDs. **Figure S2g** shows the spectra with excitation-wavelength-dependent (EWD) PL feature of N-GQD excited from 350 nm to 550 nm by a PL spectrometer. For amino-N-GQD, an emitted peak was observed at approximately 461 nm, and it shifted to approximately 605 nm with an increase in the excitation wavelength. The PL intensity decreased and showed a red-shifted PL peak. According to the above results, different types of functional groups were

introduced on the surface of N-GQDs forming "surface state" energy levels between the π and π^* states of C＝C. When radiation of a certain excitation wavelength illuminates the N-GQDs, an emissive trap of surface state dominates the emission.

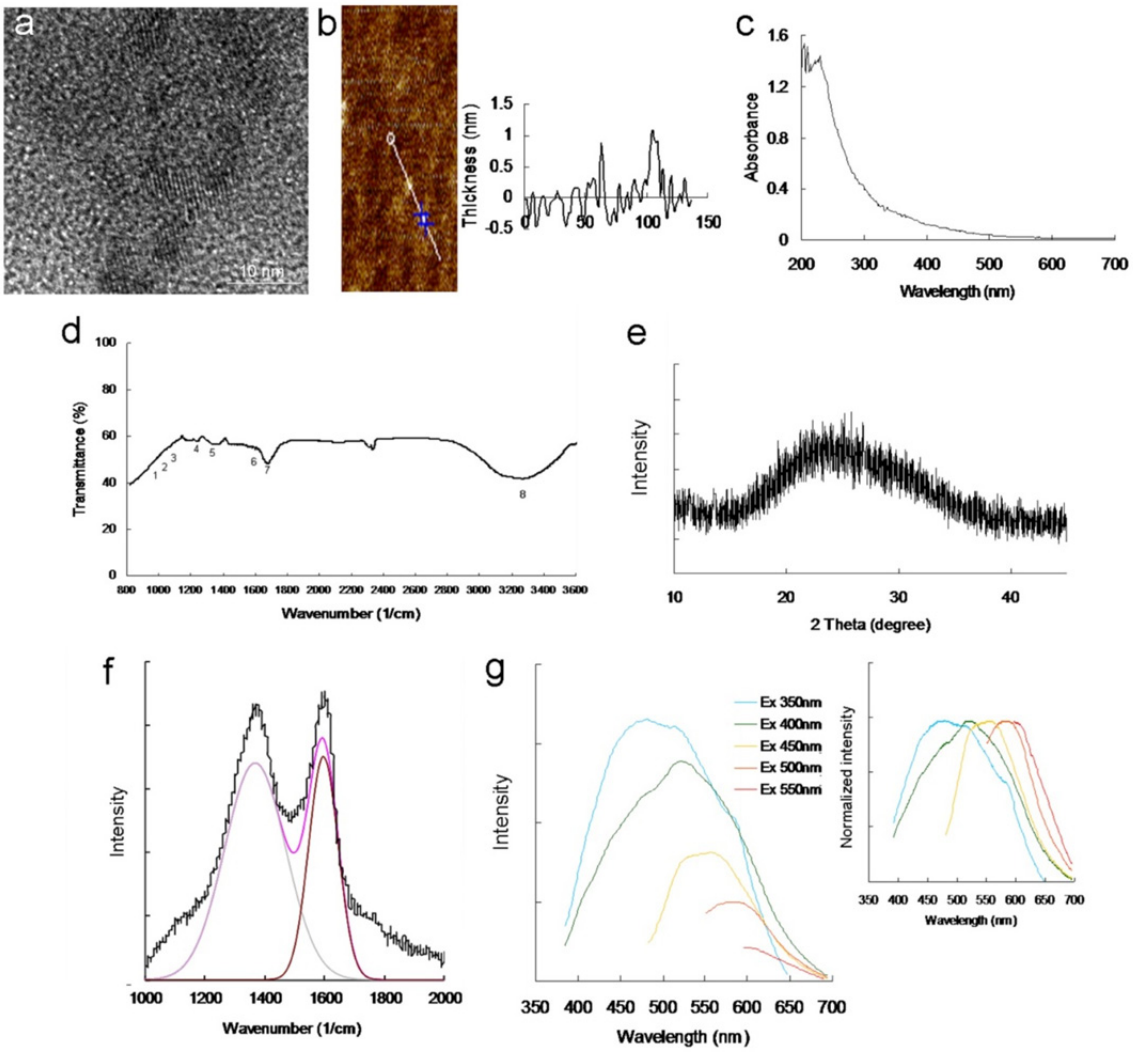

Figure S2. (a) TEM image of N-GQDs. (b) AFM image of N-GQDs on mica, and the height difference between two arrows (the N-GQDs and mica) was approximately 1.06 ± 0.05 nm. (c-g) UV-vis, FTIR, XRD, Raman and PL spectra, respectively. For Raman spectra (Excitation laser wavelength: 532nm), the deconvoluted Raman spectra and fitted peaks by using Gaussian function. The Raman spectra were decomposed into the D band and G band (black line: raw data; pink line: decomposed spectrum; gray line: D band; G band: brown line).

The surface chemistry of N-GQD was determined by XPS (**Figure S3**). The deconvoluted carbon C(1s) spectra of N-GQD were from a non-oxygenated ring (C－C/C＝C, 285.7 eV), C－N bonds (286.8 eV), hydroxyl (C－O, 287.3 eV), carbonyl (C＝O, 287.9 eV), and carboxylate (O＝C－O, 289.5 eV), respectively; the deconvoluted N(1s) spectra of N-GQD was pyridinic N (398.1 eV), pyrrolic N (399.5 eV), and quaternary N (400.9 eV), respectively. The C(1s) and N(1s) spectrum of N-GQD showed the O(1s)/C(1s) and N(1s)/C(1s) ratios to be about 38.2% and 5.1%.

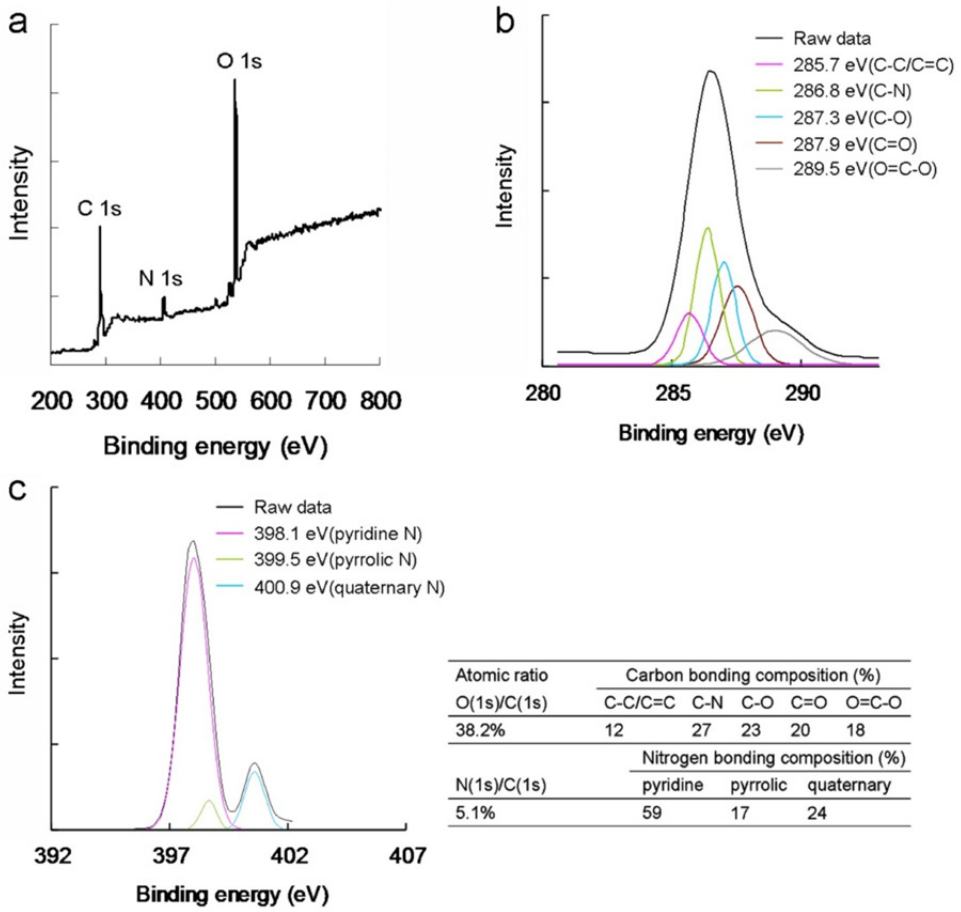

Atomic ratio	Carbon bonding composition (%)				
O(1s)/C(1s)	C-C/C=C	C-N	C-O	C=O	O=C-O
38.2%	12	27	23	20	18
	Nitrogen bonding composition (%)				
N(1s)/C(1s)	pyridine	pyrrolic	quaternary		
5.1%	59	17	24		

Figure S3. (a) Full-range XPS spectra of the N-GQDs. (b) The deconvoluted C(1s) XPS spectra and fitted peaks (using Gaussian function) for N-GQD: C－C/C＝C, C－O, C＝O, and O＝C－O. (c) N(1s) spectra and fitted peaks of XPS: pyridinic N, pyrrolic N and quaternary N. The deconvoluted C(1s) and N(1s) XPS spectra and fitted peaks by using Gaussian function. The O(1s)/C(1s) and N(1s)/C(1s) atomic ratios, C and N bonding compositions determined from the XPS for N-GQD.

Raman spectroscopy was used to monitor the inelastic phonon scattering caused by the vibration of chemical bonds which enables to calculate the size of the sp^2 domain in the sorted N-GQDs. If the mean size of the sorted N-GQDs > 3 nm, follow the Equation S10,[26]

$$L_a\ (\text{nm}) = (2.4 \times 10^{-10})\ \lambda_{laser}^{4}\ (I_D/I_G)^{-1} \quad \text{(Equation S10)}$$

where L_a (nm) is the mean size of the sp^2 domain; λ_{Laser} is the excitation wavelength (nm); I means the intensity for the D band and G band, respectively.

However, if the mean size of the sorted N-GQDs < 3 nm, follow the Equation S11,[27]

$$L_D = 0.54\ E_L^{4}\ (I_D/I_G) \quad \text{(Equation S11)}$$

where is that in small-size graphene sheets with point-like defects containing sp^3-bonded carbon atoms, the mean distance between defects, L_D (nm), is generally used to represent the size of the sp^2 domains L_D, (nm); E_{Laser} is the excitation laser energy (eV) used in Raman experiments.

The Raman spectra were obtained with a 532 nm laser and were decomposed into the D band and G band by the Lorentzian function. According to the calculations based on the Equations S10-S11, the diameter of the sorted N-GQDs was approximately 1.0 nm (compared to the N-GQD0.9 with a diameter of 0.9 nm, determined by HRTEM), 1.8 nm (compared to the N-GQD1.7 with a diameter of 1.7 nm, determined by HRTEM), 3.9 nm (compared to the N-GQD3.8 with a diameter of 3.8 nm, determined by HRTEM), 5.8 nm (compared to the N-GQD5.9 with a diameter of 5.9 nm, determined by HRTEM), 6.7 nm (compared to the N-GQD6.8 with a diameter of 6.8 nm, determined by HRTEM), 7.5 nm (compared to the N-GQD7.4 with a diameter of 7.4 nm, and 8.4 nm (compared to the N-GQD8.4 with a diameter of 8.6 nm determined by HRTEM), respectively (**Figure S4**). Results showed that the calculated values were almost consistent with that determined by HRTEM.

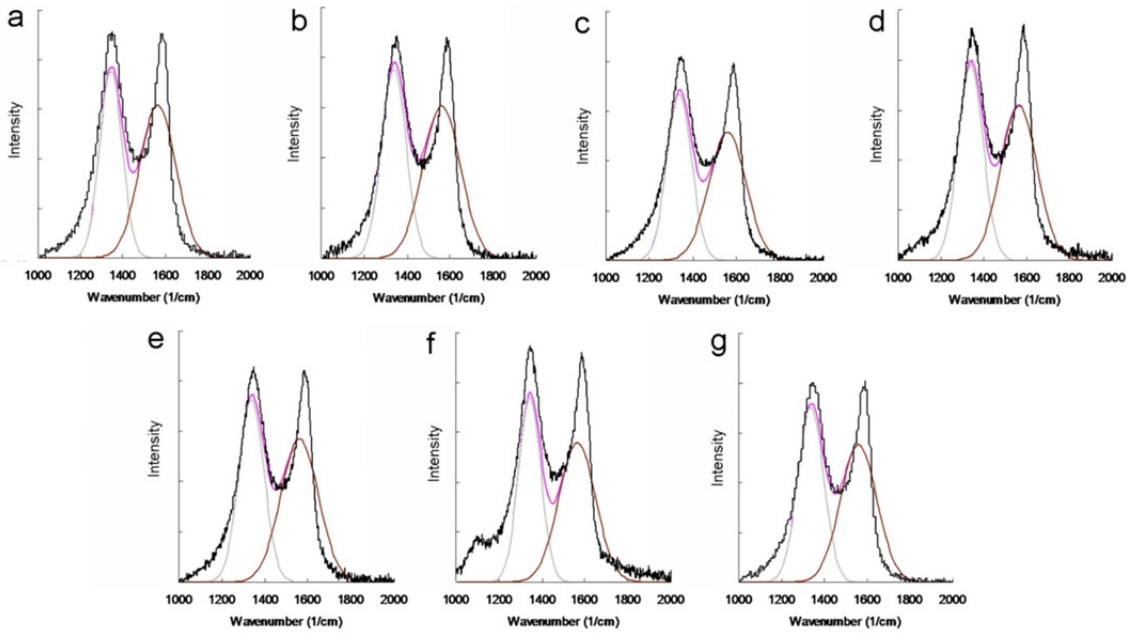

Figure S4. Raman spectra of the sorted N-GQD: (a) N-GQD0.9, (b) N-GQD1.7, (c) N-GQD3.8, (d) N-GQD 5.9, (e) N-GQD6.8, (f) N-GQD7.4, and (g) N-GQD8.4, respectively. Excitation laser wavelength: 532 nm. The deconvoluted Raman spectra and fitted peaks by using Gaussian function. The Raman spectra were decomposed into the D band and G band (black line: raw data; pink line: decomposed spectrum; gray line: D band; G band: brown line).

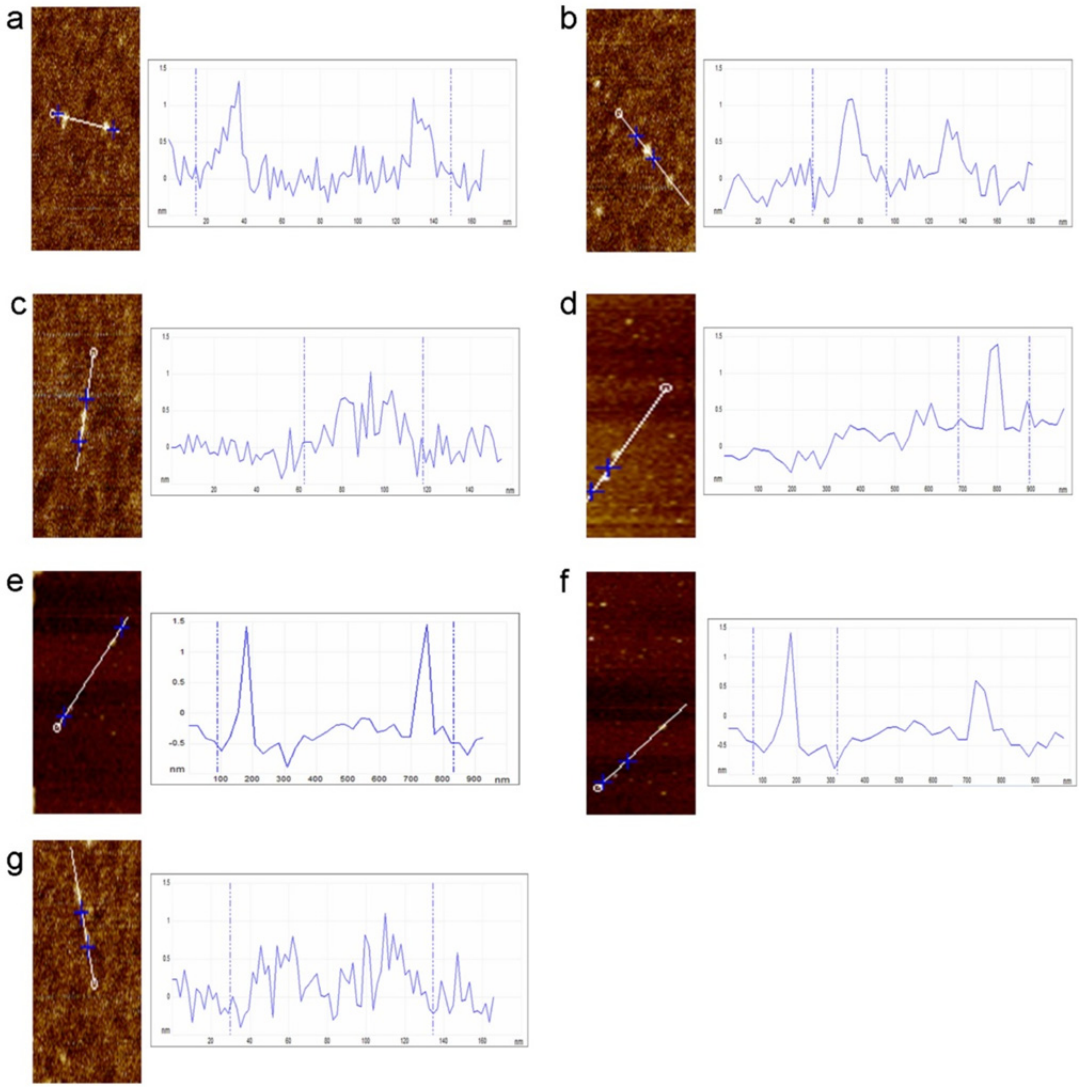

Figure S5. AFM images and height profiles of the sorted N-GQD: (a) N-GQD0.9, (b) N-GQD1.7, (c) N-GQD3.8, (d) N-GQD 5.9, (e) N-GQD6.8, (f) N-GQD7.4, and (g) N-GQD8.4, respectively.

.

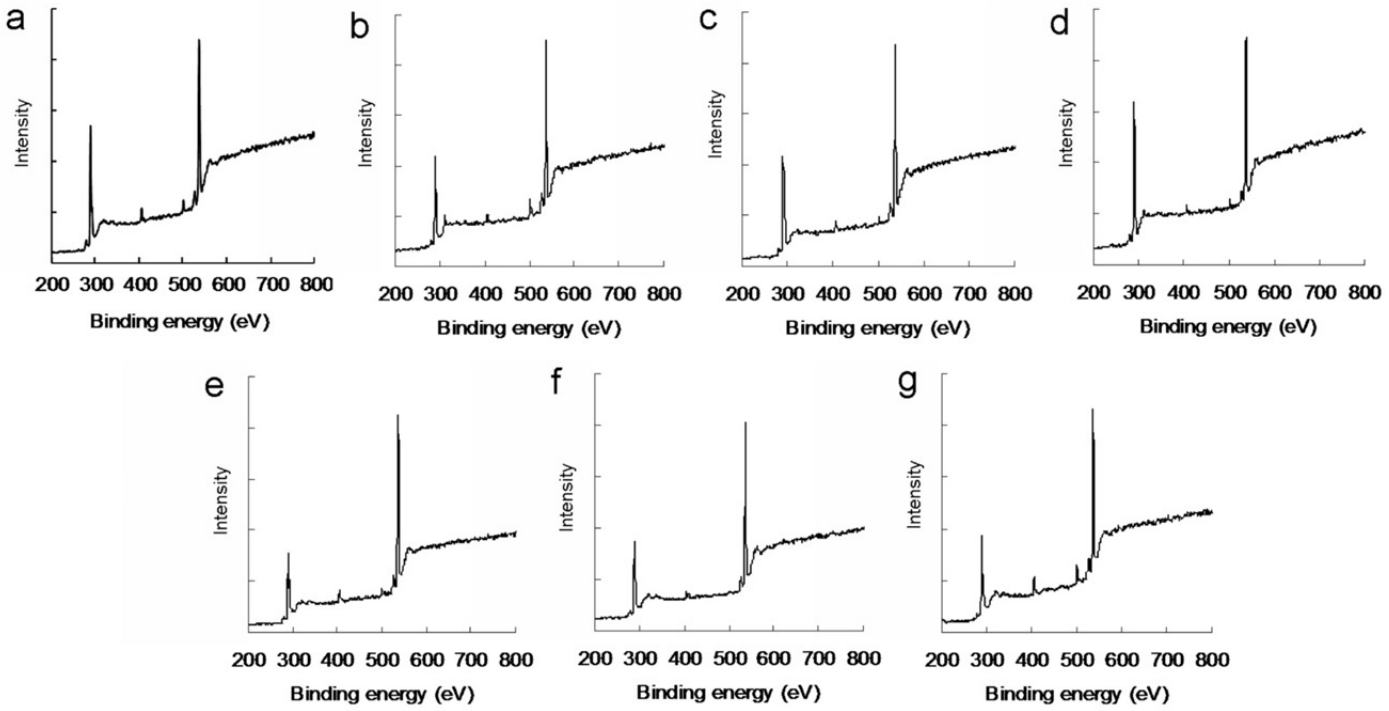

Figure S6. Full range XPS of the sorted N-GQD: (a) N-GQD0.9, (b) N-GQD1.7, (c) N-GQD3.8, (d) N-GQD 5.9, (e) N-GQD6.8, (f) N-GQD7.4, and (g) N-GQD8.4, respectively.

The deconvoluted C(1s) spectra of the sorted N-GQDs were from a non-oxygenated ring (C－C/C＝C), C－N, hydroxyl (C－O), carbonyl (C＝O), and carboxylate (O＝C－O), respectively (**Figure S7**). The C(1s) spectra of the sorted N-GQDs showed the O(1s)/C(1s) ratios to be about from 33% to 45% (**inset table, Figure S7**).

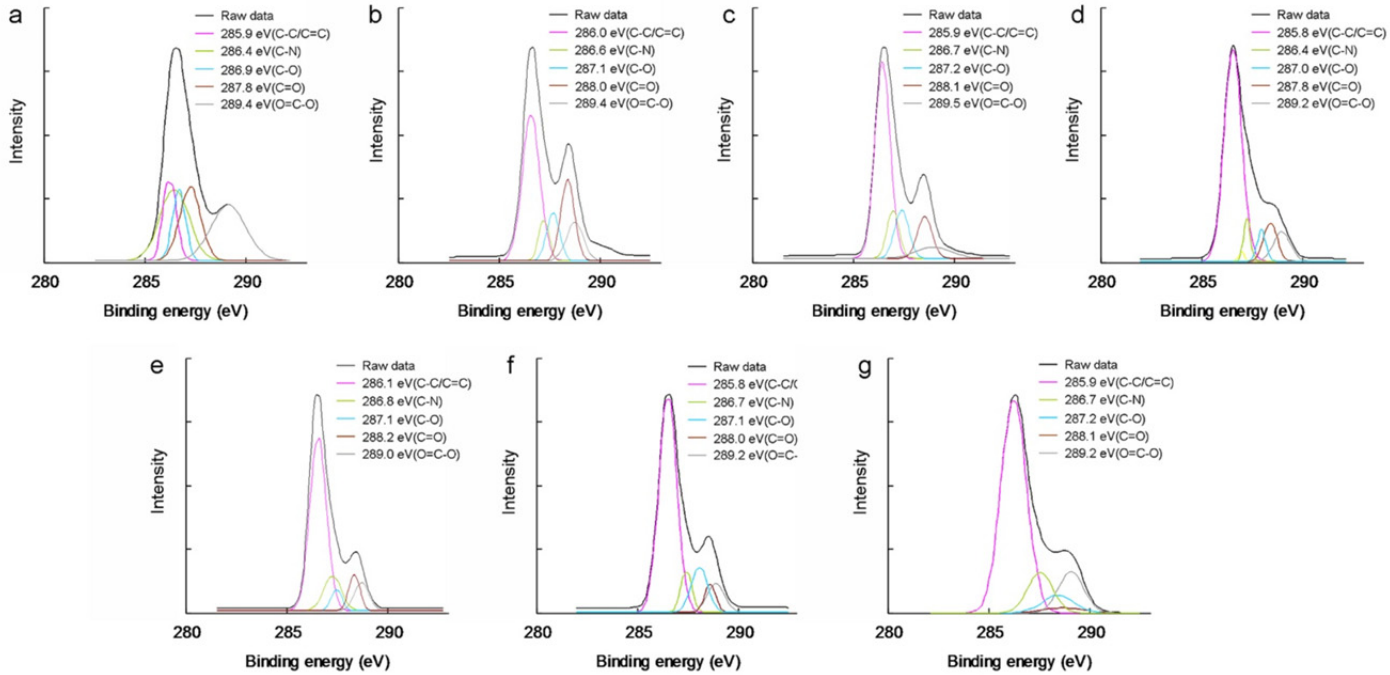

	Atomic ratio O(1s)/ C(1s)	Oxygen bonding composition (%)				
		C-C/ C=C	C-N	C-O	C=O	O=C-C
N-GQD0.9	0.33	68.6	7.4	6.3	8.5	9.2
N-GQD1.7.	0.35	70.3	7.3	6.1	8.5	7.8
N-GQD3.8	0.36	72.0	6.8	6.2	7.7	7.3
N-GQD5.9	0.38	73.2	6.6	5.9	7.4	6.9
N-GQD6.8	0.39	76.2	6.5	5.8	5.6	5.9
N-GQD7.4	0.43	80.0	5.8	5.7	4.5	4.0
N-GQD8.4	0.45	85.5	4.3	3.5	2.7	4.0

Figure S7. C (1s) XPS spectra of the sorted N-GQD: (a) N-GQD0.9, (b) N-GQD1.7, (c) N-GQD3.8, (d) N-GQD 5.9, (e) N-GQD6.8, (f) N-GQD7.4, and (g) N-GQD8.4 respectively. The deconvoluted C(1s) XPS spectra and fitted peaks by using Gaussian function.

The deconvoluted N(1s) spectra of the sorted N-GQDs were from a pyridine-N, pyrrolic-N, and quaternary-N, respectively (**Figure S8**). The N(1s) spectra of the sorted N-GQDs showed the N(1s)/C(1s) ratios to be approximately from 4.9% to 5.5% (**inset table, Figure S8**).

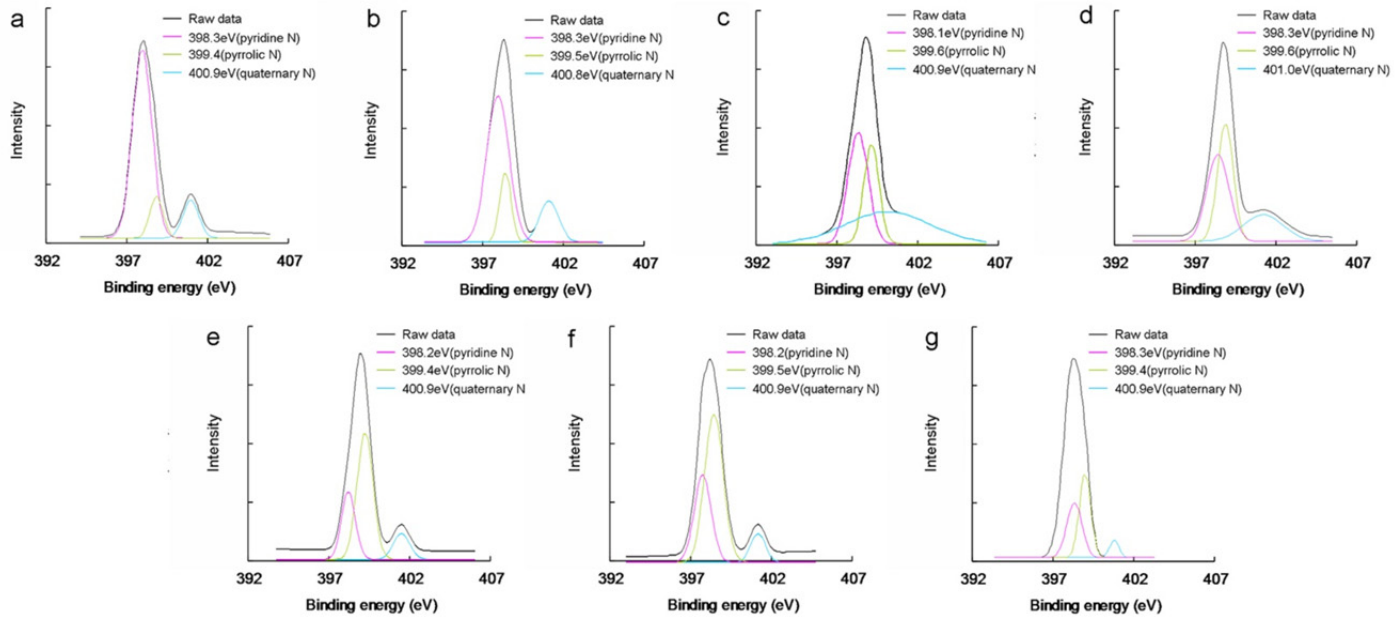

	Atomic ratio N(1s)/ C(1s)	Nitrogen bonding composition (%)		
		Pyridine	Pyrrolic	Quaternary
N-GQD0.9	0.049	47.0	25.9	27.1
N-GQD1.7.	0.052	46.4	28.2	25.4
N-GQD3.8	0.050	41.6	33.1	25.3
N-GQD5.9	0.051	38.5	39.8	21.7
N-GQD6.8	0.049	34.2	46.3	19.5
N-GQD7.4	0.054	30.3	51.5	18.2
N-GQD8.4	0.055	30.1	52.6	17.3

Figure S8. N (1s) XPS spectra of the sorted N-GQD: (a) N-GQD0.9, (b) N-GQD1.7, (c) N-GQD3.8, (d) N-GQD 5.9, (e) N-GQD6.8, (f) N-GQD7.4, and (g) N-GQD8.4, respectively. The deconvoluted N(1s) XPS spectra and fitted peaks by using Gaussian function.

FTIR was used to analyze the exposed functional groups of the sorted N-GQD (**Figure S9**). Results showed the characteristic bands of N-GQD0.9 for epoxy stretching about 1043 cm^{-1} (band 1), C－O stretching about 1110 cm^{-1} (band 2), phenolic C－OH stretching about 1197 cm^{-1} (band 3), tertiary alcoholic C－OH bending about 1350 cm^{-1} (band 4), symmetric carboxylate $C(=O)_2^-$, sp^2 C＝N and sp^3 C－N stretching about 1414, 1433 and 1449 cm^{-1} (band 5), C＝C ring stretching about 1630 cm^{-1} (band 6), C＝O stretching 1741 cm^{-1} (band 7), carboxylate O－H and N－H in-plane stretching 3219 and 3386 cm^{-1} (band 8) (**Figure S9a**); the characteristic bands of N-GQD1.7 at approximately 1047 and 1113 and 1198 cm^{-1} for epoxy, C－O and phenolic C－OH stretching (bands 1, 2 and 3), tertiary alcoholic C－OH bending about 1352 cm^{-1} (band 4), symmetric carboxylate $C(=O)_2^-$, sp^2 C＝N and sp^3 C－N stretching about 1411, 1430 and 1447 cm^{-1} (band 5), C＝C ring and C＝O stretching about 1632 and 1738 cm^{-1} (bands 6 and 7), carboxylate O－H and N－H in-plane stretching 3222 and 3384 cm^{-1} (band 8) (**Figure S9b**); the characteristic bands of N-GQD3.8 at approximately 1038 and 1108 and 1205 cm^{-1} for epoxy, C－O and phenolic C－OH stretching (bands 1, 2 and 3), tertiary alcoholic C－OH bending about 1357 cm^{-1} (band 4), symmetric carboxylate $C(=O)_2^-$, sp^2 C＝N and sp^3 C－N stretching about 1413, 1421 and 1440 cm^{-1} (band 5), C＝C ring and C＝O stretching about 1629 and 1810 cm^{-1} (bands 6 and 7), carboxylate O－H and N－H in-plane stretching 3225 and 3377 cm^{-1} (band 8) (**Figure S9c**); the characteristic bands of N-GQD5.9 at approximately 1027 and 1105 and 1211 cm^{-1} for epoxy, C－O and phenolic C－OH stretching (bands 1, 2 and 3), tertiary alcoholic C－OH bending about 1358 cm^{-1} (band 4), symmetric carboxylate $C(=O)_2^-$, sp^2 C＝N and sp^3 C－N stretching about 1415, 1422 and 1446 cm^{-1} (band 5), C＝C ring and C＝O stretching about 1609 and 1805 cm^{-1} (bands 6 and 7), carboxylate O－H and N－H in-plane stretching 3224 and 3383 cm^{-1} (band 8) (**Figure S9d**); the characteristic bands of N-GQD6.8 at approximately 1032 and 1104 and 1214 cm^{-1} for epoxy, C－O and phenolic C－OH stretching (bands 1, 2 and 3), tertiary alcoholic C－OH bending about 1364 cm^{-1} (band 4), symmetric carboxylate $C(=O)_2^-$, sp^2 C＝N and sp^3 C－N stretching about 1417, 1425 and 1433 cm^{-1} (band 5), C＝C ring and C＝O stretching about 1648 and 1739 cm^{-1} (bands 6 and 7), carboxylate O－H and N－H in-plane stretching 3220 and 3382 cm^{-1} (band 8) (**Figure S9e**); the characteristic bands of N-GQD7.4 at approximately 1033 and 1115 and 1217 cm^{-1} for epoxy, C－O and phenolic C－OH stretching (bands 1, 2 and 3), tertiary alcoholic C－OH bending about 1364 cm^{-1} (band 4), symmetric carboxylate $C(=O)_2^-$, sp^2 C＝N and sp^3 C－N stretching about 1414, 1424 and 1436 cm^{-1} (band 5), C＝C ring and C＝O stretching about 1645 and 1746 cm^{-1} (bands 6 and 7), carboxylate O－H and N－H in-plane stretching 3228 and 3389 cm^{-1} (band 8) (**Figure S9f**); the characteristic bands of N-GQD8.4 at approximately 1021 and 1135 and 1222 cm^{-1} for epoxy, C－O and phenolic C－OH stretching (bands 1, 2 and 3), tertiary alcoholic C－OH bending about 1370 cm^{-1} (band 4), symmetric carboxylate $C(=O)_2^-$, sp^2 C＝N and sp^3 C－N stretching about 1409, 1431 and 1446 cm^{-1} (band 5), C＝C ring and C＝O stretching about 1629 and 1733 cm^{-1} (bands 6 and 7), carboxylate O－H and N－H in-plane stretching 3232 and 3380 cm^{-1} (band 8) (**Figure S9g**).The results indicated the functional groups of carboxyl, hydroxyl and epoxy were exposed from the sorted N-GQDs.

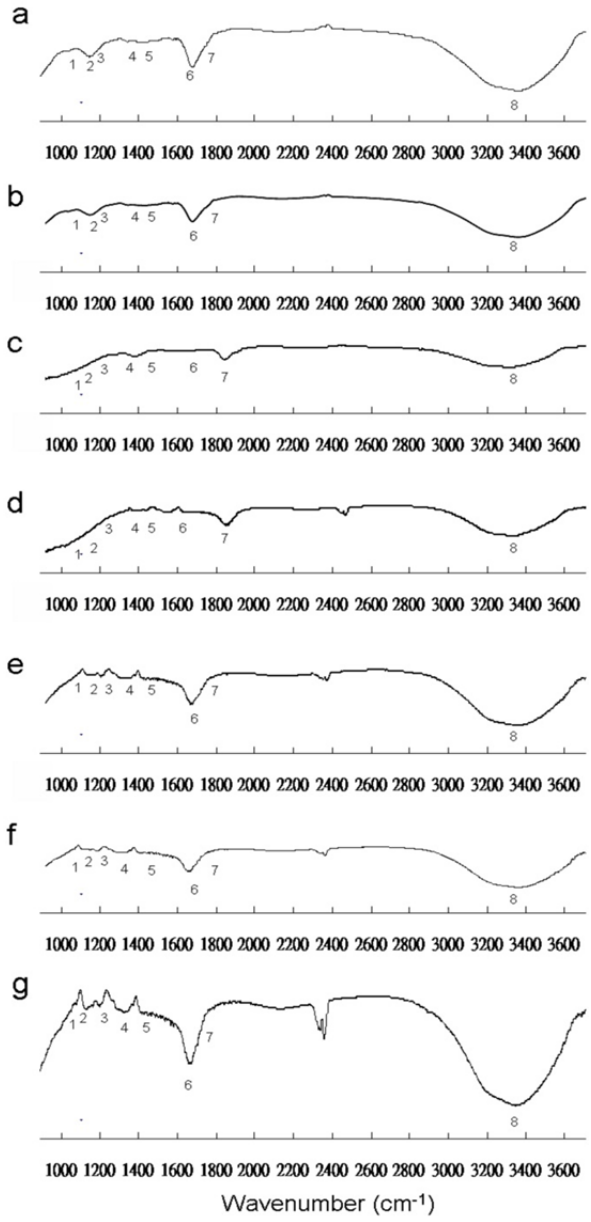

Figure S9. FTIR spectra of the sorted N-GQD: (a) N-GQD0.9, (b) N-GQD1.7, (c) N-GQD3.8, (d) N-GQD 5.9, (e) N-GQD6.8, (f) N-GQD7.4, and (g) N-GQD8.4, respectively.

Table S1. The surface charge of the materials was confirmed by the zeta-potential spectroscopy.

Zeta potential (mV)	N-GQD 0.9	N-GQD 1.7	N-GQD 3.8	N-GQD 5.9	N-GQD 6.8	N-GQD 7.4	N-GQD 8.4
	-17.5	-17.8	-16.1	-17.3	-15.7	-16.9	-16.3
	N-GQD -PEI1.1	N-GQD -PEI2.0	N-GQD -PEI4.2	N-GQD -PEI6.3	N-GQD -PEI7.1	N-GQD -PEI7.7	N-GQD -PEI8.6
	14.6	14.9	15.2	16.0	15.4	16.5	16.7

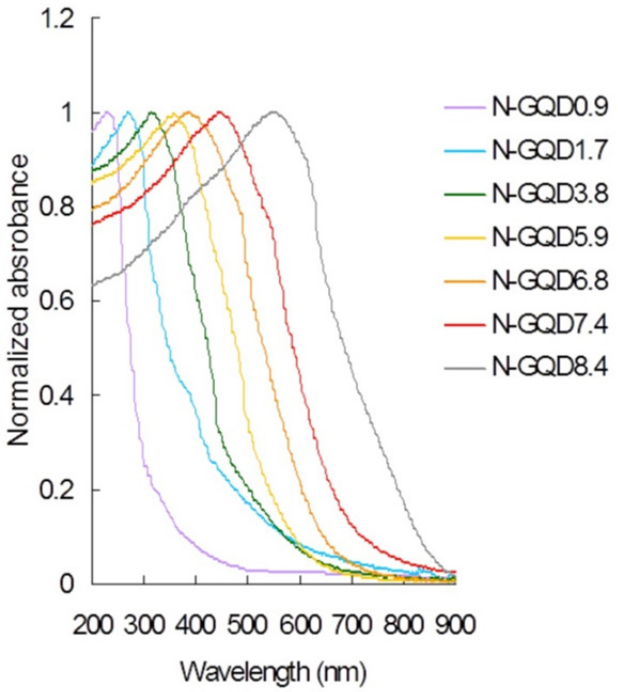

Figure S10. UV-vis spectra of the sorted N-GQDs. Material dose delivered: 5 μg mL^{-1}.

The sorted N-GQDs emitted peak were observed at approximately 384 nm (N-GQD0.9), 450 nm (N-GQD1.7), 504 nm (N-GQD3.8), 549 nm (N-GQD5.9), 592 nm (N-GQD6.8), 626 nm (N-GQD7.4) and 690 nm (N-GQD8.4), respectively, with the excitation wavelength encompassed from UV to NIR window. The sorted N-GQDs showed the phenomenon of excitation-wavelength-dependent PL emission (**Figure S11**).

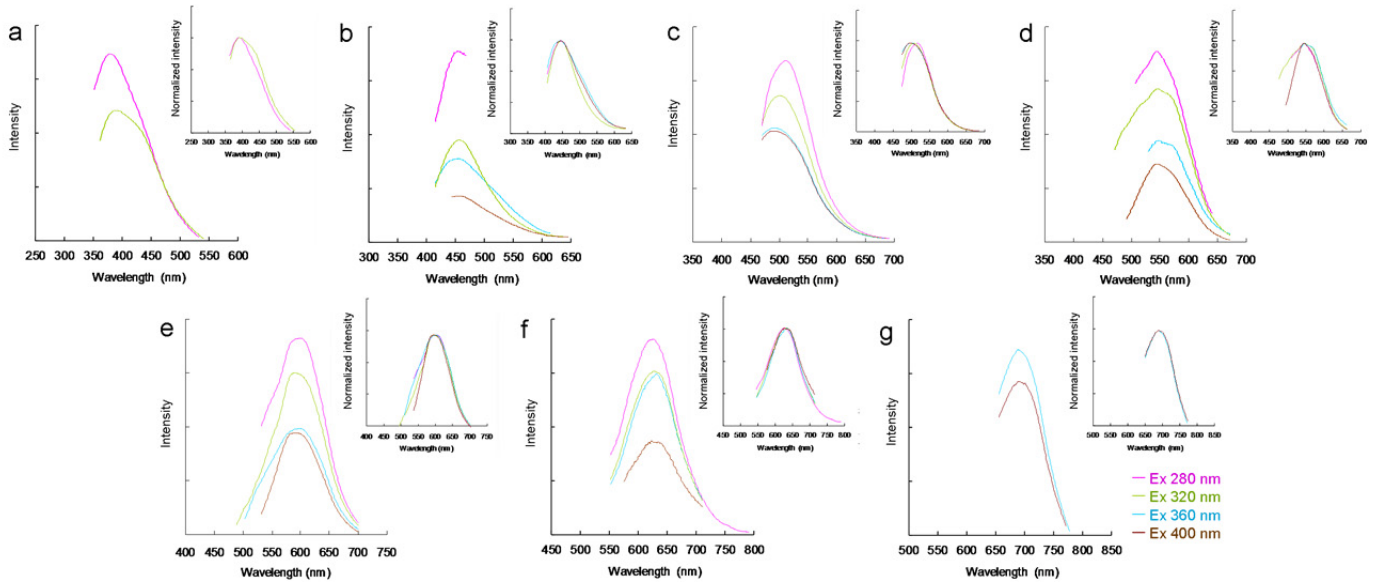

Figure S11. Spectra with excitation-wavelength-independent (EWI) PL feature of the sorted N-GQD: (a) N-GQD0.9, (b) N-GQD1.7, (c) N-GQD3.8, (d) N-GQD 5.9, (e) N-GQD6.8, (f) N-GQD7.4, and (g) N-GQD8.4, respectively.

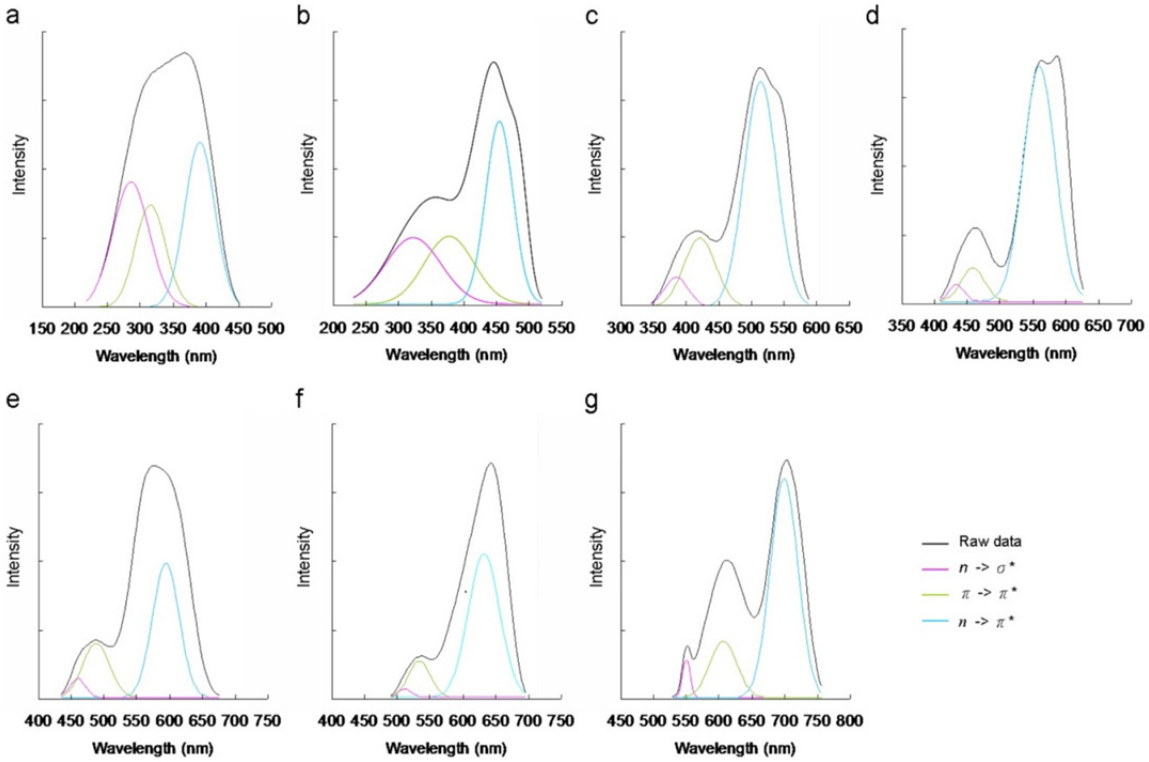

Figure S12. Photoluminescence excitation (PLE) spectra of aqueous dispersions of (a) N-GQD0.9, (b) N-GQD1.7, (c) N-GQD3.8, (d) N-GQD 5.9, (e) N-GQD6.8, (f) N-GQD7.4, and (g) N-GQD8.4, respectively. Spectra, which can be deconvoluted into three peaks of $n \rightarrow \sigma^*$, $\pi \rightarrow \pi^*$, and $n \rightarrow \pi^*$ corresponding to electron transitions, were determined by the wavelengths of the maximal PL emissions in **Figure S11**.

To identify the valence band edges (*i.e.*, the *n*-state, denoted as E_v) of the sorted N-GQDs, we respectively deposited them on the silicon substrate and determined the E_v by using UPS with He I light (21.2 eV) irradiation. The following Equation S11 was used for UPS analysis[28]:

$$E_B + E_k + \varphi = 21.2 \text{ eV} \quad \text{(Equation S11)}$$

where E_B is the binding energy measured from the Fermi level, E_k is the kinetic energy of electrons, φ is the work function of the sorted N-GQDs, and 21.2 eV is the energy of the He I light. The *E*v can be calculated using the following Equation S12[29]:

$$E_v = 21.2 \text{ eV} - (E_{B2} - E_{B1}) \quad \text{(Equation S12)}$$

where E_{B2} is the secondary cutoff binding energy in the UPS spectra, in which the E_k of the excited electrons is equal to 0; E_{B1} represents the difference between the Fermi edges and the valence band edges.[30] **Figure S13** shows the UPS spectra of the sorted N-GQDs. The E_{B1} can be determined using the intercepts of the extrapolated straight lines on the abscissa at low binding energy. The E_{B2} can be estimated using the secondary cutoff values (E_k = 0 eV) in the UPS spectra, obtained from the intercepts of the extrapolated straight lines on the abscissa at high binding energy. The UPS widths are the difference between E_{B2} and E_{B1}. The E_v can be calculated by subtracting these UPS widths from the excitation energy (21.2 eV).

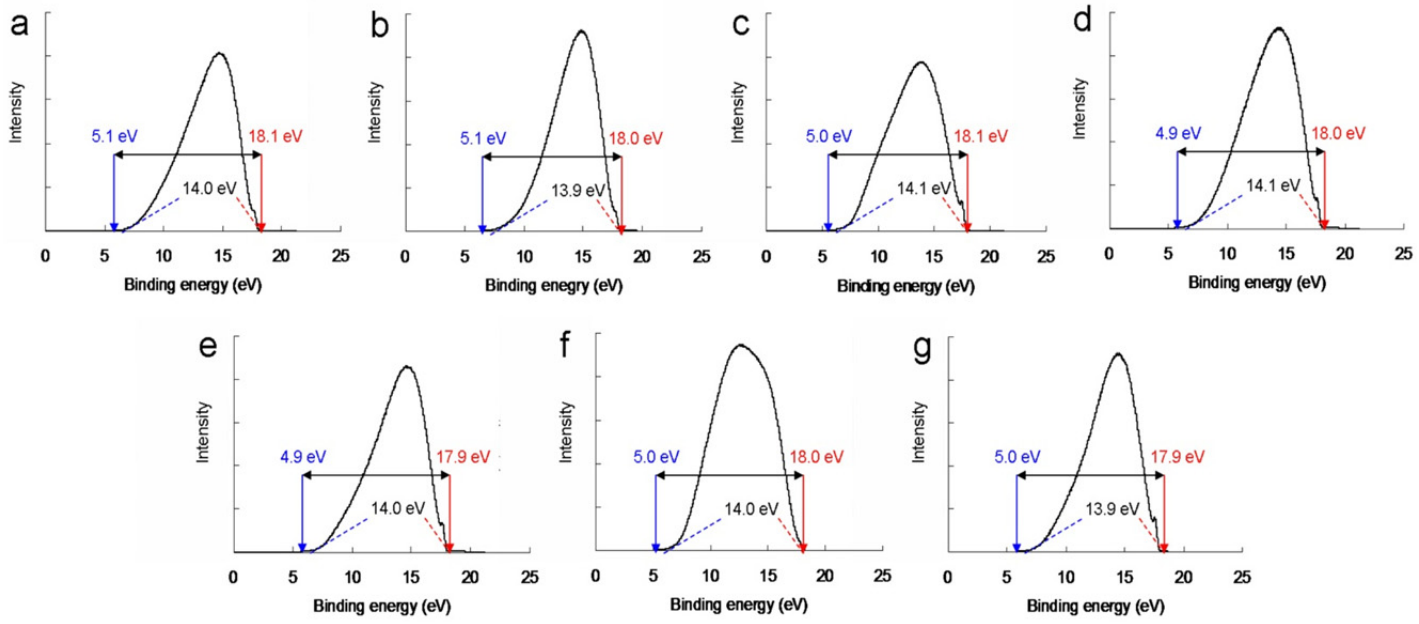

Figure S13. UPS spectra of (a) N-GQD0.9, (b) N-GQD1.7, (c) N-GQD3.8, (d) N-GQD 5.9, (e) N-GQD6.8, (f) N-GQD7.4, and (g) N-GQD8.4, respectively. The valence band levels with respect to the Fermi levels were determined from the intercepts of the extrapolated straight lines (blue dashed line) on the abscissa at low binding energy. The intersections of the tangent (red dashed line) with the abscissa at high binding energy give the secondary onset binding energy. The UPS widths (black lines) can be determined from these two binding energies, and the valence band edges can be calculated by subtracting these widths from the excitation energy (21.2 eV).

Figure S14 shows a schematic of the energy levels associated with the absorption and PL of the sorted N-GQDs. We located the *n*-state level (*i.e.*, the highest occupied orbital level) of each sorted N-GQD on the basis of the UPS analysis (**Figure S13**). The *n*-state levels of the specimens were located at similar energetic positions. The energy values required for the $n \rightarrow \pi^*$, $\pi \rightarrow \pi^*$, and $n \rightarrow \sigma^*$ transitions in each sorted N-GQD specimen (**Figure S12**) were used to determine the levels of the π, π^*, and σ^* states on the basis of the identified *n*-state level. The EWI-PL emissions were ascribed to the $\pi^* \rightarrow n$ transition.[30] The PLE spectra depict an energy difference between the absorptive $n \rightarrow \pi^*$ and radiative $\pi^* \rightarrow n$ transitions. This energy difference cannot be attributed to the relaxation of electrons to shallow trap states below the π^* level because the presence of trap states generally results in EWD emissions. Instead, the energy level diagram in **Figure S14** shows that the transition of electrons from the π^* orbital to the *n*-state orbital for radiative recombination involves energy loss through phonon scattering for achieving momentum alignment, although we cannot rule out the possibility of other relaxation mechanisms causing the energy difference. Because the PL emissions were EWI, electrons excited to the σ^* orbital relaxed to the π^* orbital for radiative $\pi^* \rightarrow n$ recombination.

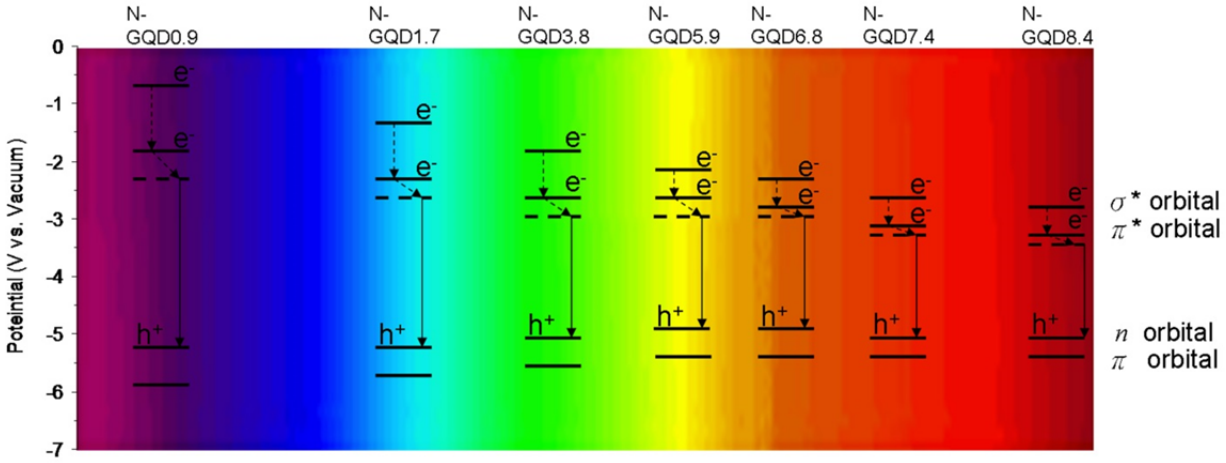

Figure S14. Schematic energy level diagram for the sorted N-GQDs. A schematic of the energy levels associated with size-dependent PL emissions from the sorted N-GQDs. The energy levels are determined on the basis of PLE (**Figure S12**) and UPS (**Figure S13**) analysis. The level of the *n*-states is not disturbed by a change in the particle size, whereas the levels of theπ, π^*, and σ^* orbitals vary considerably with the size. The $\pi^* \rightarrow n$ recombination, which involves phonon scattering and an electron transition, is responsible for the EWI-PL in the sorted N-GQDs. The relaxation of electrons from the σ^* orbital to the π^* orbital is essential for PL emissions induced by short-wavelength excitation. The PL color varies from UV (for N-GQD0.9) to NIR (for N-GQD8.4).

Raman spectra were obtained with a 532 nm laser and were decomposed into the D band and G band by the Lorentzian function. According to the calculations based on the Equations S10-S11, the diameter of the sorted N-GQD-PEI was approximately 1.1 nm (N-GQD-PEI1.1), 2.0 nm (N-GQD-PEI2.0), 4.2 nm (N-GQD-PEI4.2), 6.3 nm (N-GQD-PEI6.3), 7.1 nm (N-GQD-PEI7.1), 7.7 nm (N-GQD-PEI7.7) and 8.6 nm (N-GQD-PEI8.6), respectively (**Figure S15**).

After conjugation with PEI on the surface of the sorted N-GQDs, the position of the D band and G band for N-GQD-PEI1.1 (**Figure S15a**) was shifted from 1386 cm^{-1} to 1372 cm^{-1} and from 1605 cm^{-1} to 1593 cm^{-1}, compared with **Figure S4a**, respectively; the position of the D band and G band for N-GQD-PEI2.0 (**Figure S15b**) was shifted from 1386 cm^{-1} to 1373 cm^{-1} and from 1607 cm^{-1} to 1595 cm^{-1}, compared with **Figure S4b**, respectively; the position of the D band and G band for N-GQD-PEI4.2 (**Figure S15c**) was shifted from 1385 cm^{-1} to 1371 cm^{-1} and from 1605 cm^{-1} to 1594 cm^{-1}, compared with **Figure S4c**, respectively; the position of the D band and G band for N-GQD-PEI6.3 (**Figure S15d**) was shifted from 1385 cm^{-1} to 1370 cm^{-1} and from 1604 cm^{-1} to 1592 cm^{-1}, compared with **Figure S4d,** respectively; the position of the D band and G band for N-GQD-PEI7.1 (**Figure S15e**) was shifted from 1387 cm^{-1} to 1371 cm^{-1} and from 1607 cm^{-1} to 1593 cm^{-1}, compared with **Figure S4e**, respectively; the position of the D band and G band for N-GQD-PEI7.7 (**Figure S15f**) was shifted from 1386 cm^{-1} to 1370 cm^{-1} and from 1605 cm^{-1} to 1592 cm^{-1}, compared with **Figure S4f**, respectively; the position of the D band and G band for N-GQD-PEI8.4 (**Figure S15g**) was shifted from 1385 cm^{-1} to 1371 cm^{-1} and from 1606 cm^{-1} to 1592 cm^{-1}, compared with **Figure S4g**, respectively. Probably due to the electron-donor molecule of PEI, resulting in high-frequency-PEI to shift to lower frequencies.[31]

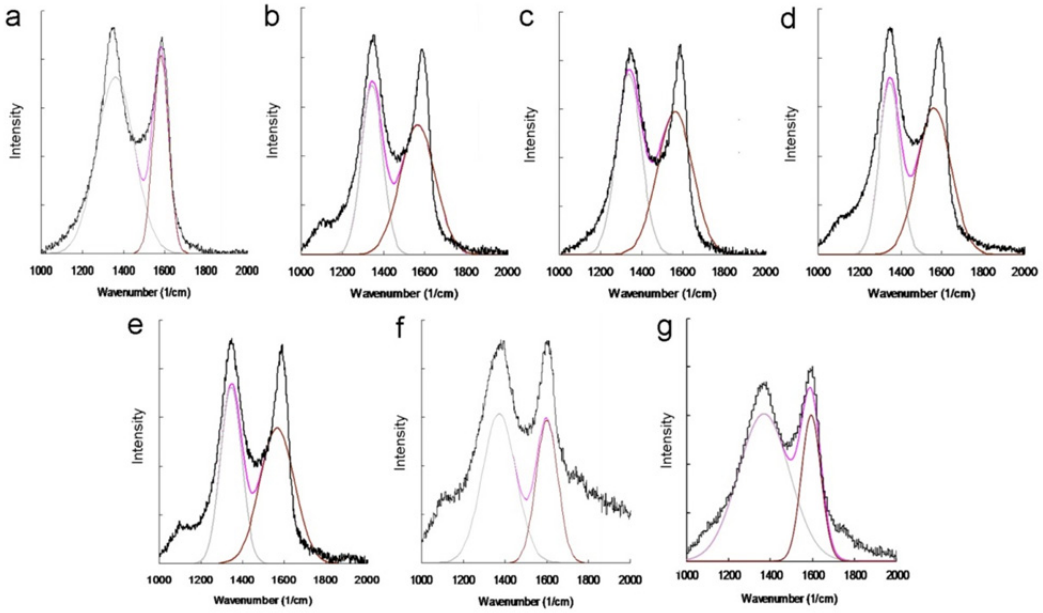

Figure S15. Raman spectra of (a) N-GQD-PEI1.1, (b) N-GQD-PEI2.0, (c) N-GQD-PEI4.2, (d) N-GQD-PEI6.3, (e) N-GQD-PEI7.1, (f) N-GQD-PEI7.7 and (g) N-GQD-PEI8.6, respectively. Excitation laser wavelength: 532nm. The deconvoluted Raman spectra and fitted peaks by using Gaussian function. The Raman spectra were decomposed into the D band and G band (black line: raw data; pink line: decomposed spectrum; gray line: D band; G band: brown line).

FTIR was used to analyze the exposed functional groups of the N-GQD-polymers (**Figure S16**). Results showed characteristic bands of N-GQD-PEI1.1 for C－N stretching about 1084 cm^{-1} and 1137 cm^{-1} (band 1 and 2), C－H bending about 1325 cm^{-1} (band 3), N－H bending about 1492 cm^{-1} (band 4), N－H scissor about 1686 cm^{-1} (band 5), broad N－H stretching 2405 cm^{-1} (band 6), C－H stretching about 2819 cm^{-1} (band 7), and N－H stretching 3342 cm^{-1} (band 8) (**Figure S16a**); the characteristic bands of N-GQD-PEI2.0 at approximately 1071 and 1123 cm^{-1} for C－N stretching (band 1 and 2), C－H bending about 1322 cm^{-1} (band 3), N－H bending about 1496 cm^{-1} (band 4), N－H scissor about 1672 cm^{-1} (band 5), broad N－H stretching 2409 cm^{-1} (band 6), C－H stretching about 2813 cm^{-1} (band 7), and N－H stretching 3329 cm^{-1} (band 8) (**Figure S16b**); the characteristic bands of N-GQD-PEI4.2 at approximately 1069 and 1127 cm^{-1} for C－N stretching (band 1 and 2), C－H bending about 1328 cm^{-1} (band 3), N－H bending about 1473 cm^{-1} (band 4), N－H scissor about 1665 cm^{-1} (band 5), broad N－H stretching 2418 cm^{-1} (band 6), C－H stretching about 2834 cm^{-1} (band 7), and N－H stretching 3337 cm^{-1} (band 8) (**Figure S16c**); the characteristic bands of N-GQD-PEI6.3 at approximately 1063 and 1128 cm^{-1} for C－N stretching (band 1 and 2), C－H bending about 1331 cm^{-1} (band 3), N－H bending about 1478 cm^{-1} (band 4), N－H scissor about 1669 cm^{-1} (band 5), broad N－H stretching 2420 cm^{-1} (band 6), C－H stretching about 2827 cm^{-1} (band 7), and N－H stretching 3331 cm^{-1} (band 8) (**Figure S16d**); the characteristic bands of N-GQD-PEI7.1 at approximately 1066 and 1124 cm^{-1} for C－N stretching (band 1 and 2), C－H bending about 1335 cm^{-1} (band 3), N－H bending about 1468 cm^{-1} (band 4), N－H scissor about 1637 cm^{-1} (band 5), broad N－H stretching 2388 cm^{-1} (band 6), C－H stretching about 2807 cm^{-1} (band 7), and N－H stretching 3334 cm^{-1} (band 8) (**Figure S16e**); the characteristic bands of N-GQD-PEI7.7 at approximately 1060 and 1118 cm^{-1} for C－N stretching (band 1 and 2), C－H bending about 1326 cm^{-1} (band 3), N－H bending about 1463 cm^{-1} (band 4), N－H scissor about 1662 cm^{-1} (band 5), broad N－H stretching 2397 cm^{-1} (band 6), C－H stretching about 2806 cm^{-1} (band 7), and N－H stretching 3327 cm^{-1} (band 8) (**Figure S16f**); the characteristic bands of N-GQD-PEI8.6 at approximately 1054 and 1117 cm^{-1} for C－N stretching (band 1 and 2), C－H bending about 1333 cm^{-1} (band 3), N－H bending about 1467 cm^{-1} (band 4), N－H scissor about 1660 cm^{-1} (band 5), broad N－H stretching 2404 cm^{-1} (band 6), C－H stretching about 2809 cm^{-1} (band 7), and N－H stretching 3332 cm^{-1} (band 8) (**Figure S16g**). The results indicated the polymer of PEI was conjugated on the surface of the sorted N-GQDs.

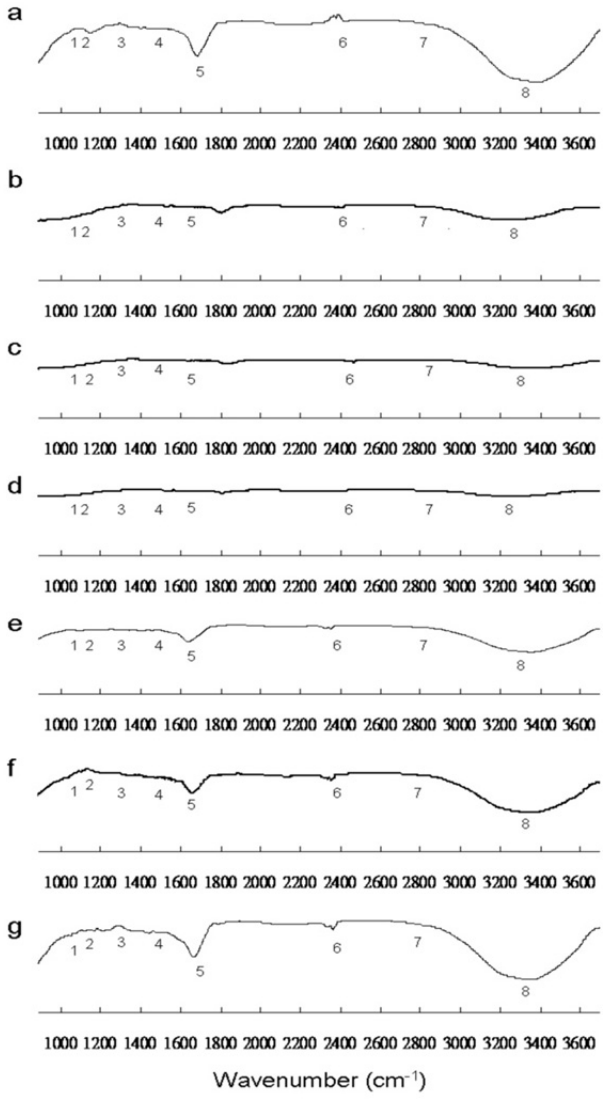

Figure S16. FTIR spectra of (a) N-GQD-PEI1.1, (b) N-GQD-PEI2.0, (c) N-GQD-PEI4.2, (d) N-GQD-PEI6.3, (e) N-GQD-PEI7.1, (f) N-GQD-PEI7.7 and (g) N-GQD-PEI8.6, respectively.

Table S2. Stability of the newly prepared and as-prepared sorted-N-GQD-PEI for 3 months in physiological environment of the culture medium for A549 cancer cell determined by Raman and zeta potential spectroscopy.

Mean lateral size (nm)/ Zeta potential (mV)	Newly prepared	As-prepare for 3 months
N-GQD-PEI1.1	1.1 / 14.6	1.2 / 14.7
N-GQD-PEI2.0	2.0 / 14.9	2.1 / 14.5
N-GQD-PEI4.2	4.2 / 15.2	4.1 / 15.6
N-GQD-PEI6.3	6.3 / 16.0	6.3 / 15.9
N-GQD-PEI7.1	7.1 / 15.4	7.0 / 15.7
N-GQD-PEI7.7	7.7 / 16.5	7.8 / 16.8
N-GQD-PEI8.6	8.6 / 16.7	8.7 / 16.9

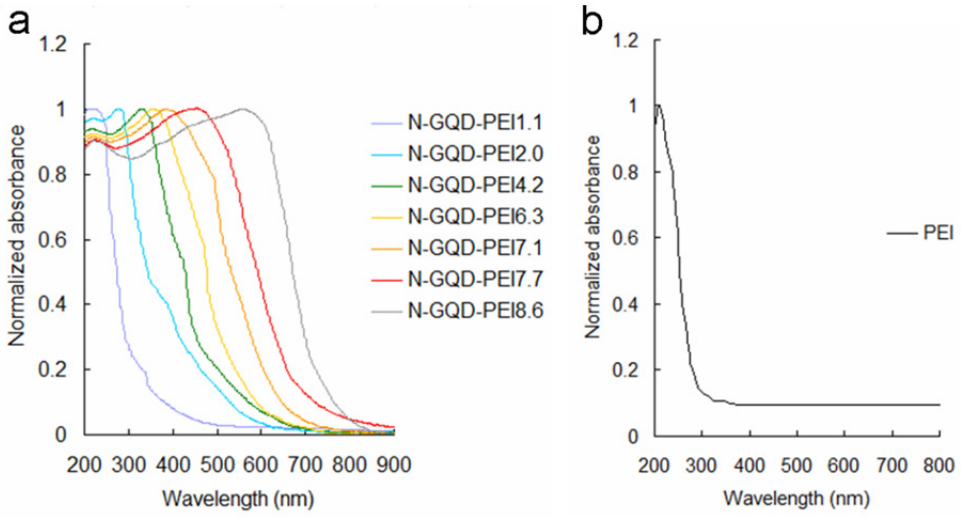

Figure S17. UV–vis spectra of (a) sorted N-GQD-PEI materials and (b) PEI. The PEI characteristic peak was observed at approximately 208 nm. For N-GQD-PEI1.1, N-GQD-PEI2.0, N-GQD-PEI4.2, N-GQD-PEI6.3, N-GQD-PEI7.1, N-GQD-PEI7.7, and N-GQD-PEI8.6, the wavelengths of the normalized maximal absorbance were approximately 228, 273, 320, 359, 382, 446, and 553 nm, respectively—which were attributed to the π–π* transition aromatic C=C bonds (sp^2 domains)—and the wavelengths of the edge absorbance were approximately 325, 386, 423, 471, 488, 551, and 614 nm, respectively—which were assigned to the n–π* transition of the C=O shoulder and C–N. Material dose delivered: 5 μg mL^{-1}.

The sorted N-GQDs emitted peak were observed at approximately 393 nm (N-GQD-PEI1.1), 462 nm (N-GQD-PEI2.0), 518 nm (N-GQD-PEI4.2), 560 nm (N-GQD-PEI6.3), 605 nm (N-GQD-PEI7.1), 636 nm (N-GQD-PEI7.7) and 698 nm (N-GQD-PEI8.6), respectively, with the excitation wavelength encompassed from UV to NIR window (**Figure S18**).

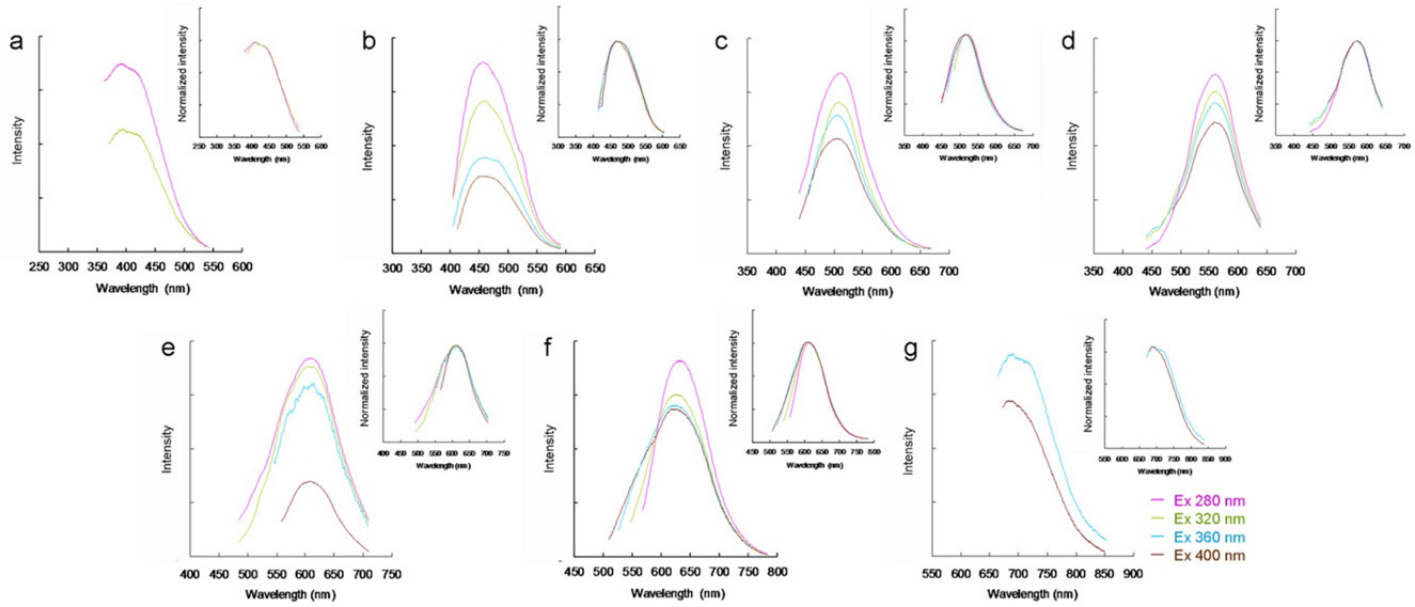

Figure S18. Spectra with EWI-PL feature of (a) N-GQD-PEI1.1, (b) N-GQD-PEI2.0, (c) N-GQD-PEI4.2, (d) N-GQD-PEI6.3, (e) N-GQD-PEI7.1, (f) N-GQD-PEI7.7 and (g) N-GQD-PEI8.6, respectively.

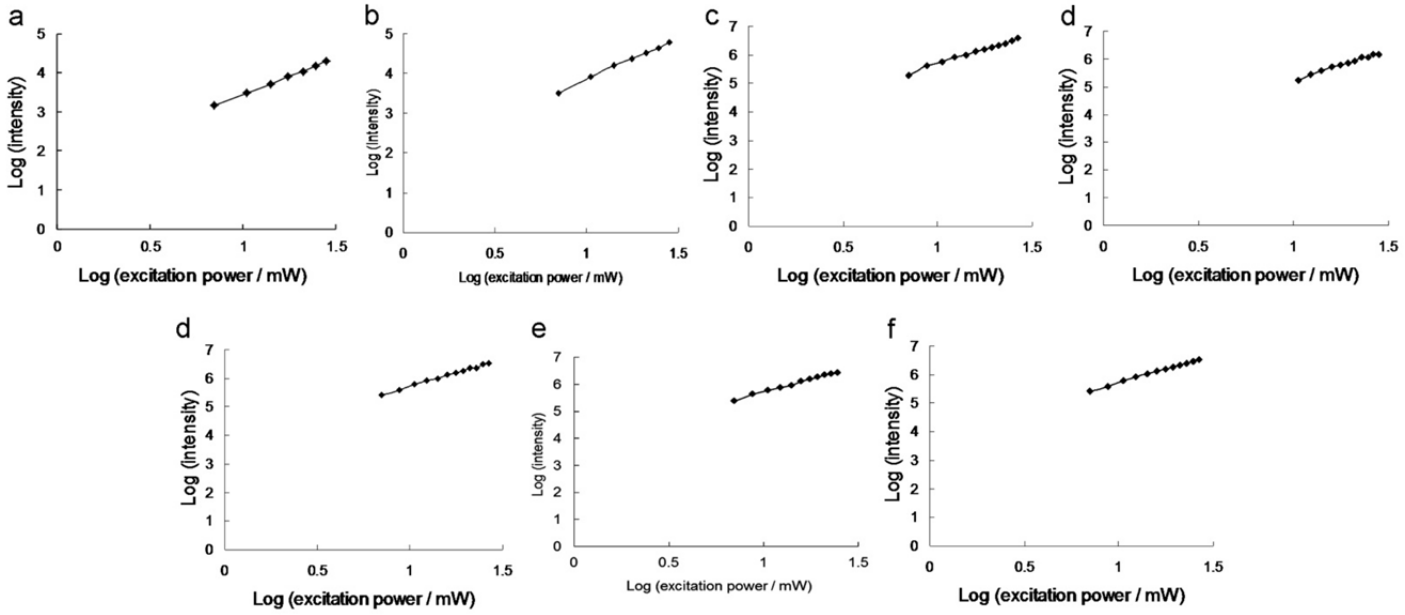

Figure S19. The TPL intensity dependence on the excitation power (logarithm) of (a) N-GQD-PEI1.1, (b) N-GQD-PEI2.0, (c) N-GQD-PEI4.2, (d) N-GQD-PEI6.3, (e) N-GQD-PEI7.1, (f) N-GQD-PEI7.7 and (g) N-GQD-PEI8.6 with slopes of 2.00, 1.99, 2.02, 1.98, 2.01, 1.99 and 2.00, respectively, exposed to 704 nJ pixel^{-1} to 2816 nJ pixel^{-1} of TPE. R^2> 0.99 (Ex: 800 nm). Delivered dose of material: 0.25 μg mL^{-1}.

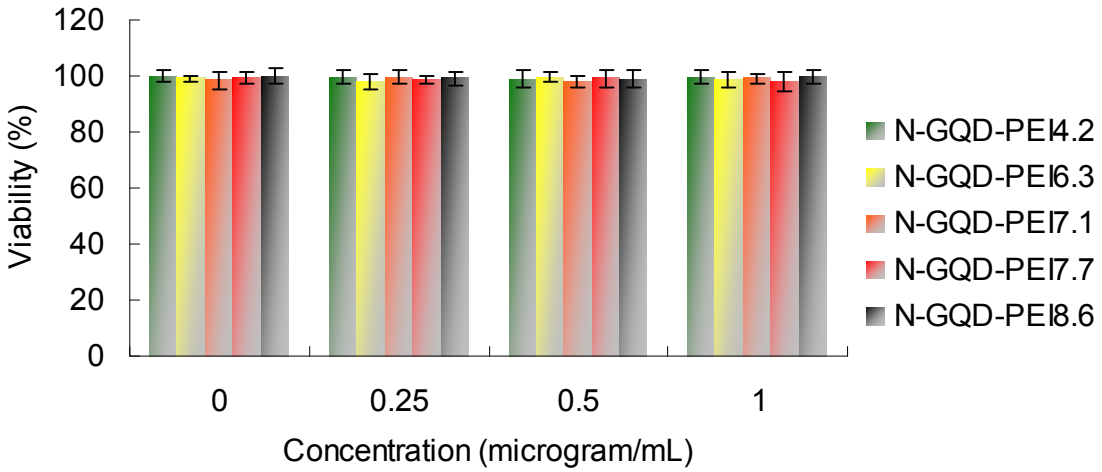

Figure S20. A549 cells were incubated with the sorted N-GQD-PEI-Ab_{EGFR} in the dark for 24h and then the viability was evaluated by MTT assay.

Table S3. The amount of ROS generated from at a TPE power of 14.7 nJ pixel^{-1} for 6 min (approximately 79470 scans) to N-GQD-PEI4.2-Ab_{EGFR} or -$Ab_{microtubule}$ (0.25 μg mL^{-1})-treated-A549 was monitored. Ex: 800 nm. Data are means ± SD (n=6).

			$^1O_2$ (by SOSG)[c]			
Negative control[ac]	ROS neutralization[abc]	Positive control[cd]	N-GQD-PEI 4.2-Ab_{EGFR}	ROS neutralization[bc]	N-GQD-PEI 4.2-$Ab_{microtubule}$	ROS neutralization[bc]
228±13	232±16	6021±183	233±17	232±14	235±17	233±15
			$^1O_2$ (by *t*-MVP)[e]			
Negative control[ae]	ROS neutralization[abe]	Positive control[de]	N-GQD-PEI 4.2-Ab_{EGFR}	ROS. neutralization[be]	N-GQD-PEI 4.2-$Ab_{microtubule}$	ROS neutralization[be]
349±15	352±18	9267±266	353±18	351±17	354±17	352±15
			$O_2 \bullet^-$ (by XTT)[f]			
Negative control[af]	ROS neutralization[abf]	Positive control[df]	N-GQD-PEI 4.2-Ab_{EGFR}	ROS neutralization[bf]	N-GQD-PEI 4.2-$Ab_{microtubule}$	ROS neutralization[bf]
0	0	0.95±0.07	0.03±0.01	0.03±0.01	0.03±0.02	0.03±0.01
			$O_2 \bullet^-$ (by GSH)[g]			
Negative control[ag]	ROS neutralization[abg]	Positive control[dg]	N-GQD-PEI 4.2-Ab_{EGFR}	ROS neutralization[bg]	N-GQD-PEI 4.2-$Ab_{microtubule}$	ROS neutralization[bg]
0	0	99.8±0.6%	0.3±0.1%	0.3±0.1%	0.3±0.1%	0.2±0.1%

[a]Negative control: only treat reagent and laser irradiation without material (0 μg mL^{-1}).

[b]ROS neutralization: with the treatments of nanomaterial, the laser irradiation and 30 ppm of antioxidant α-Tocopherol/methyl linoleate.[15,16]

[c]SOSG reagent (Ex/Em: 488/525 nm)[4,5,17] has a specific reactivity to generate fluorescence recorded by a PL spectrometer.

[d]Positive control: the treatment of 50 μM *tert*-butyl hydroperoxide (TBHP)[32] and laser irradiation.

[e]*t*-MVP (Ex/Em: 352/465 nm)[18] can react with $^1O_2$, forming a dioxetane intermediate that generates fluorescence upon decomposition to 1-pyrenecarboxaldehyde, and monitored by a PL spectrometer.

[f]XTT would interact with $O_2^{\bullet-}$ and produce the XTT-formazan generating strong absorption (470 nm in wavelength).[19,20]

[g]GSH containing a thiol-tripeptide can prevent damages to cellular or bacterial components caused by stress of oxidation.[21-23] Thiol group from GSH can be oxidized to disulfide bond converting GSH to glutathione disulfide. GSH oxidation was used to determine the generated $O_2^{\bullet-}$. Loss of GSH (%) = (absorbance difference between of sample and negative control / absorbance of negative control) × 100 %.

Table S4. The amount of ROS generated at a TPE power of 14.7 nJ pixel^{-1} for 6 min (approximately 79470 scans) to N-GQD-PEI6.3-Ab_{EGFR} or -$Ab_{mitochondrion}$ (0.25 μg mL^{-1})-treated-A549 was monitored. Ex: 800 nm. Data are means ± SD (n=6).

			$^1O_2$ (by SOSG)[c]			
Negative control[ac]	ROS neutralization[abc]	Positive control[cd]	N-GQD-PEI 6.3-Ab_{EGFR}	ROS neutralization[bc]	N-GQD-PEI 6.3-$Ab_{mitochondrion}$	ROS neutralization[bc]
231±19	233±16	5904±138	235±15	232±12	234±14	233±14
			$^1O_2$ (by *t*-MVP)[e]			
Negative control[ae]	ROS neutralization[abe]	Positive control[de]	N-GQD-PEI 6.3-Ab_{EGFR}	ROS neutralization[be]	N-GQD-PEI 6.3-$Ab_{mitochondrion}$	ROS neutralization[be]
358±20	356±18	9105±248	357±19	354±17	355±16	355±15
			$O_2 \bullet^-$ (by XTT)[f]			
Negative control[af]	ROS neutralization[abf]	Positive control[df]	N-GQD-PEI 6.3-Ab_{EGFR}	ROS neutralization[bf]	N-GQD-PEI 6.3-$Ab_{mitochondrion}$	ROS neutralization[bf]
0	0	0.92±0.04	0.04±0.02	0.03±0.02	0.03±0.01	0.03±0.01
			$O_2 \bullet^-$ (by GSH)[g]			
Negative control[ag]	ROS neutralization[abg]	Positive control[dg]	N-GQD-PEI 6.3-Ab_{EGFR}	ROS neutralization[bg]	N-GQD-PEI 6.3-$Ab_{mitochondrion}$	ROS neutralization[bg]
0	0	99.5±1.0%	0.2±0.1%	0.2±0.1%	0.3±0.1%	0.2±0.2%

[a]Negative control: only treat reagent and laser irradiation without material (0 μg mL^{-1}).

[b]ROS neutralization: with the treatments of nanomaterial, the laser irradiation and 30 ppm of antioxidant α-Tocopherol/methyl linoleate.[15,16]

[c]SOSG reagent (Ex/Em: 488/525 nm)[4,5,17] has a specific reactivity to generate fluorescence recorded by a PL spectrometer.

[d]Positive control: the treatment of 50 μM TBHP[32] and laser irradiation.

[e]*t*-MVP (Ex/Em: 352/465 nm)[18] can react with $^1O_2$, forming a dioxetane intermediate that generates fluorescence upon decomposition to 1-pyrenecarboxaldehyde, and monitored by a PL spectrometer.

[f]XTT would interact with $O_2^{\bullet -}$ and produce the XTT-formazan generating strong absorption (470 nm in wavelength).[19,20]

[g]GSH containing a thiol-tripeptide can prevent damages to cellular or bacterial components caused by stress of oxidation.[21-23] Thiol group from GSH can be oxidized to disulfide bond converting GSH to glutathione disulfide. GSH oxidation was used to determine the generated $O_2^{\bullet -}$. Loss of GSH (%) = (absorbance difference between of sample and negative control / absorbance of negative control) × 100 %.

Table S5. The amount of ROS generated from at a TPE power of 14.7 nJ pixel^{-1} for 6 min (approximately 79470 scans) to N-GQD-PEI7.1-Ab_{EGFR} or -Ab_{golgi} (0.25 μg mL^{-1})-treated-A549 was monitored. Ex: 800 nm. Data are means ± SD (n=6).

			$^1O_2$ (by SOSG)[c]			
Negative control[ac]	ROS neutralization[abc]	Positive control[cd]	N-GQD-PEI 7.1-Ab_{EGFR}	ROS neutralization[bc]	N-GQD-PEI 7.1-Ab_{golgi}	ROS neutralization[bc]
230±15	228±12	5937±169	232±16	230±14	231±15	227±10
			$^1O_2$ (by *t*-MVP)[e]			
Negative control[ae]	ROS neutralization[abe]	Positive control[de]	N-GQD-PEI 7.1-Ab_{EGFR}	ROS neutralization[be]	N-GQD-PEI 7.1-Ab_{golgi}	ROS neutralization[be]
352±13	357±16	9198±226	356±15	350±11	354±15	351±12
			$O_2 \bullet^-$ (by XTT)[f]			
Negative control[af]	ROS neutralization[abf]	Positive control[df]	N-GQD-PEI 7.1-Ab_{EGFR}	ROS neutralization[bf]	N-GQD-PEI 7.1-Ab_{golgi}	ROS neutralization[bf]
0	0	0.96±0.05	0.03±0.02	0.03±0.01	0.03±0.01	0.02±0.01
			$O_2 \bullet^-$ (by GSH)[g]			
Negative control[ag]	ROS neutralization[abg]	Positive control[dg]	N-GQD-PEI 7.1-Ab_{EGFR}	ROS neutralization[bg]	N-GQD-PEI 7.1-Ab_{golgi}	ROS neutralization[bg]
0	0	99.4±1.0%	0.3±0.2%	0.3±0.1%	0.2±0.1%	0.2±0.1%

[a]Negative control: only treat reagent and laser irradiation without material (0 μg mL^{-1}).

[b]ROS neutralization: with the treatments of nanomaterial, the laser irradiation and 30 ppm of antioxidant α-Tocopherol/methyl linoleate.[15,16]

[c]SOSG reagent (Ex/Em: 488/525 nm)[4,5,17] has a specific reactivity to generate fluorescence recorded by a PL spectrometer.

[d]Positive control: the treatment of 50 μM TBHP[32] and laser irradiation.

[e]*t*-MVP (Ex/Em: 352/465 nm)[18] can react with $^1O_2$, forming a dioxetane intermediate that generates fluorescence upon decomposition to 1-pyrenecarboxaldehyde, and monitored by a PL spectrometer.

[f]XTT would interact with $O_2^{\bullet-}$ and produce the XTT-formazan generating strong absorption (470 nm in wavelength).[19,20]

[g]GSH containing a thiol-tripeptide can prevent damages to cellular or bacterial components caused by stress of oxidation.[21-23] Thiol group from GSH can be oxidized to disulfide bond converting GSH to glutathione disulfide. GSH oxidation was used to determine the generated $O_2^{\bullet-}$. Loss of GSH (%) = (absorbance difference between of sample and negative control / absorbance of negative control) × 100 %.

Table S6. The amount of ROS generated at a TPE power of 14.7 nJ pixel^{-1} for 6 min (approximately 79470 scans) to N-GQD-PEI7.7-Ab_{EGFR} or -$Ab_{nucleus}$ (0.25 μg mL^{-1})-treated-A549 was monitored. Ex: 800 nm. Data are means ± SD (n=6).

			$^1O_2$ (by SOSG)[c]			
Negative control[ac]	ROS neutralization[abc]	Positive control[cd]	N-GQD-PEI 7.7-Ab_{EGFR}	ROS neutralization[bc]	N-GQD-PEI 7.7-$Ab_{nucleus}$	ROS neutralization[bc]
227±13	230±14	5997±175	234±15	229±14	232±15	230±13
			$^1O_2$ (by *t*-MVP)[e]			
Negative control[ae]	ROS neutralization[abe]	Positive control[de]	N-GQD-PEI 7.7-Ab_{EGFR}	ROS neutralization[be]	N-GQD-PEI 7.7-$Ab_{nucleus}$	ROS neutralization[be]
361±13	355±17	9221±206	355±18	355±18	354±17	354±18
			$O_2 \bullet^-$ (by XTT)[f]			
Negative control[af]	ROS neutralization[abf]	Positive control[df]	N-GQD-PEI 7.7-Ab_{EGFR}	ROS neutralization[bf]	N-GQD-PEI 7.7-$Ab_{nucleus}$	ROS neutralization[bf]
0	0	0.93±0.08	0.03±0.01	0.02±0.01	0.03±0.01	0.03±0.01
			$O_2 \bullet^-$ (by GSH)[g]			
Negative control[ag]	ROS neutralization[abg]	Positive control[dg]	N-GQD-PEI 7.7-Ab_{EGFR}	ROS neutralization[bg]	N-GQD-PEI 7.7-$Ab_{nucleus}$	ROS neutralization[bg]
0	0	99.8±0.9%	0.4±01%	0.2±0.1%	0.3±0.1%	0.3±0.1%

[a]Negative control: only treat reagent and laser irradiation without material (0 μg mL^{-1}).

[b]ROS neutralization: with the treatments of nanomaterial, the laser irradiation and 30 ppm of antioxidant α-Tocopherol/methyl linoleate.[15,16]

[c]SOSG reagent (Ex/Em: 488/525 nm)[4,5,17] has a specific reactivity to generate fluorescence recorded by a PL spectrometer.

[d]Positive control: the treatment of 50 μM TBHP[32] and laser irradiation.

[e]*t*-MVP (Ex/Em: 352/465 nm)[18] can react with $^1O_2$, forming a dioxetane intermediate that generates fluorescence upon decomposition to 1-pyrenecarboxaldehyde, and monitored by a PL spectrometer.

[f]XTT would interact with $O_2^{\bullet -}$ and produce the XTT-formazan generating strong absorption (470 nm in wavelength).[19,20]

[g]GSH containing a thiol-tripeptide can prevent damages to cellular or bacterial components caused by stress of oxidation.[21-23] Thiol group from GSH can be oxidized to disulfide bond converting GSH to glutathione disulfide. GSH oxidation was used to determine the generated $O_2^{\bullet -}$. Loss of GSH (%) = (absorbance difference between of sample and negative control / absorbance of negative control) × 100 %.

Table S7. The amount of ROS generated at a TPE power of 14.7 nJ pixel^{-1} for 6 min (approximately 79470 scans) to N-GQD-PEI8.6-Ab_{EGFR} or -Ab_{ER} (0.25 μg mL^{-1})-treated-A549 was monitored. Ex: 800 nm. Data are means ± SD (n=6).

			$^1O_2$ (by SOSG)[c]			
Negative control[ac]	ROS neutralization[abc]	Positive control[cd]	N-GQD-PEI 8.6-Ab_{EGFR}	ROS neutralization[bc]	N-GQD-PEI 8.6-Ab_{ER}	ROS neutralization[bc]
233±12	234±11	5954±147	232±11	232±14	233±12	233±10
			$^1O_2$ (by *t*-MVP)[e]			
Negative control[ae]	ROS neutralization[abe]	Positive control[de]	N-GQD-PEI 8.6-Ab_{EGFR}	ROS neutralization[be]	N-GQD-PEI 8.6-Ab_{ER}	ROS neutralization[be]
355±12	356±15	9188±210	354±15	356±14	355±12	355±14
			$O_2 \bullet^-$ (by XTT)[f]			
Negative control[af]	ROS neutralization[abf]	Positive control[df]	N-GQD-PEI 8.6-Ab_{EGFR}	ROS neutralization[bf]	N-GQD-PEI 8.6-Ab_{ER}	ROS neutralization[bf]
0	0	0.94±0.06	0.02±0.01	0.02±0.02	0.02±0.01	0.02±0.01
			$O_2 \bullet^-$ (by GSH)[g]			
Negative control[ag]	ROS neutralization[abg]	Positive control[dg]	N-GQD-PEI 8.6-Ab_{EGFR}	ROS neutralization[bg]	N-GQD-PEI 8.6-Ab_{ER}	ROS neutralization[bg]
0	0	99.7±0.7%	0.2±0.1%	0.3±0.1%	0.3±0.2%	0.2±0.1%

[a]Negative control: only treat reagent and laser irradiation without material (0 μg mL^{-1}).

[b]ROS neutralization: with the treatments of nanomaterial, the laser irradiation and 30 ppm of antioxidant α-Tocopherol/methyl linoleate.[15,16]

[c]SOSG reagent (Ex/Em: 488/525 nm)[4,5,17] has a specific reactivity to generate fluorescence recorded by a PL spectrometer.

[d]Positive control: the treatment of 50 μM TBHP[32] and laser irradiation.

[e]*t*-MVP (Ex/Em: 352/465 nm)[18] can react with $^1O_2$, forming a dioxetane intermediate that generates fluorescence upon decomposition to 1-pyrenecarboxaldehyde, and monitored by a PL spectrometer.

[f]XTT would interact with $O_2^{\bullet-}$ and produce the XTT-formazan generating strong absorption (470 nm in wavelength).[19,20]

[g]GSH containing a thiol-tripeptide can prevent damages to cellular or bacterial components caused by stress of oxidation.[21-23] Thiol group from GSH can be oxidized to disulfide bond converting GSH to glutathione disulfide. GSH oxidation was used to determine the generated $O_2^{\bullet-}$. Loss of GSH (%) = (absorbance difference between of sample and negative control / absorbance of negative control) × 100 %.

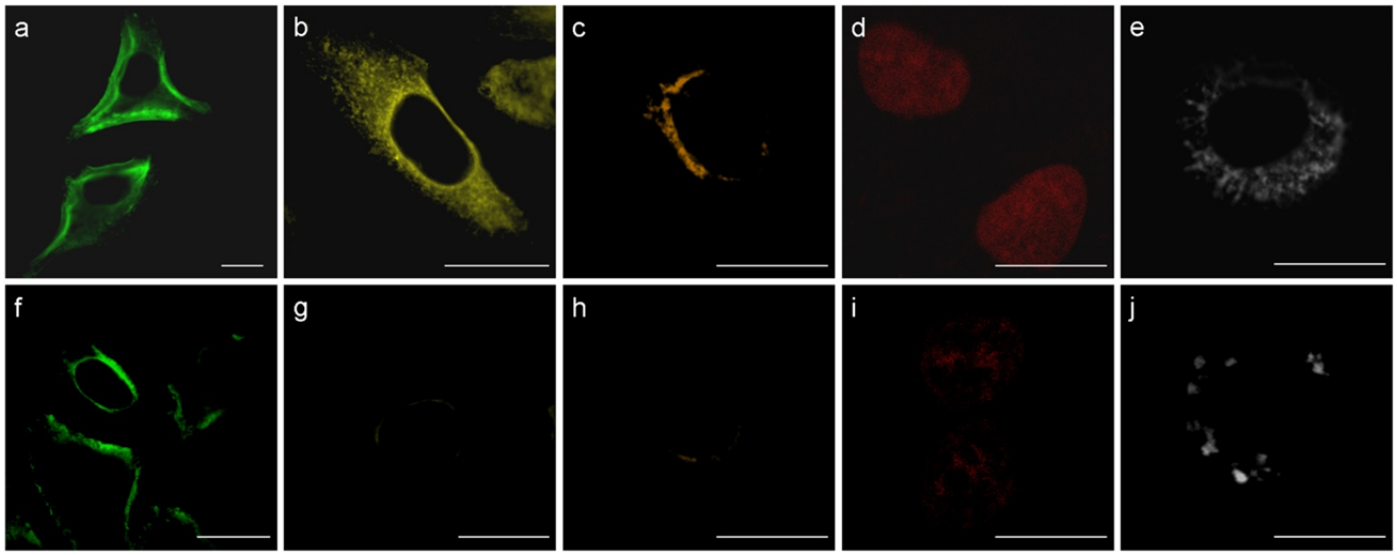

Figure S21. Images of TPL captured at (a) N-GQD-PEI4.2-$Ab_{microtubule}$-, (b) N-GQD-PEI6.3-$Ab_{mitochrondrion}$-, (c) N-GQD-PEI7.1-Ab_{golgi}-, (d) N-GQD-PEI7.7-$Ab_{nucleus}$-, (e) N-GQD-PEI8.6-Ab_{ER}-, (f) $Ab_{microtubule}$ (tubulin, YOL1/34)-Alexa Fluor 488- (abcam, Cambridge, UK), (g) $Ab_{mitochrodrion}$ (COX IV)-Alexa Fluor 546- (abcam, Cambridge, UK), (h) Ab_{golgi} (GM130)-Alexa Fluor 594- (abcam, Cambridge, UK), (i) $Ab_{nucleus}$ (Lamin B1)-Alexa Fluor 660- (abcam, Cambridge, UK), and (j) Ab_{ER}(KDEL)-Alexa Fluor 680- (abcam, Cambridge, UK)-treated A549 cell at the depth of 110 μm and at a TPE power of 14.7 nJ $pixel^{-1}$ with 66225 scans (approximately 2 min). Material dose delivered: 0.25 μg mL^{-1}. Excitation wavelength: 800 nm. Scale bar: 10 μm.

As a function of TPE time (0-6 min), the relative intensity of integrated area from 350 nm to 700 nm in wavelength of TPL maintained almost the same intensity, exhibiting the highly photostability of the sorted N-GQD-PEI-Ab (**Figure S22**).

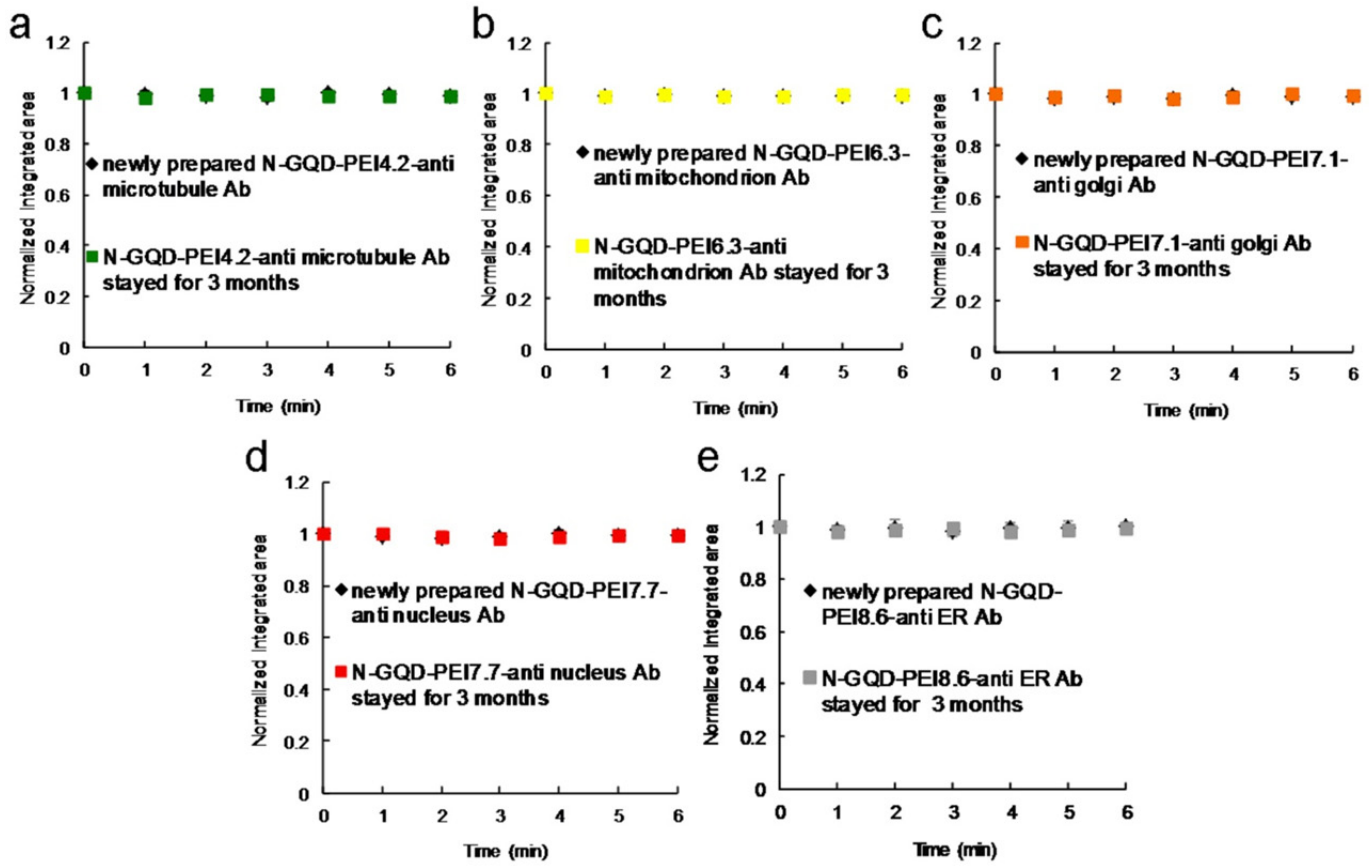

Figure S22. Photostability of (a) N-GQD-PEI4.2-$Ab_{microtubule}$, (b) N-GQD-PEI6.3-$Ab_{mitochrondrion}$, (c) N-GQD-PEI7.1-Ab_{golgi}, (d) N-GQD-PEI7.7-$Ab_{nucleus}$, and (e) N-GQD-PEI8.6-Ab_{ER} which was subjected to TPE at 14.7 nJ $pixel^{-1}$ for 6 min (approximately 79470 scans). Other emission intensities of integrated area after photoexcitation were respectively divided into that of newly prepared sorted-N-GQDs-PEI-Ab without photoexcitation, leading to obtain the normalized integrated area. Ex: 800 nm. Delivered dose of material: 0.25 μg mL^{-1}. Data shown are means ± SD (n = 6).

As a function of TPE time (0-6 min), the relative intensity of integrated area from 450 nm to 700 nm in wavelength of TPL decayed the same intensity, exhibiting the low photostability of the commercially conventional fluorophores (Ab-Alexa Fluor dyes) (**Figure S23**).

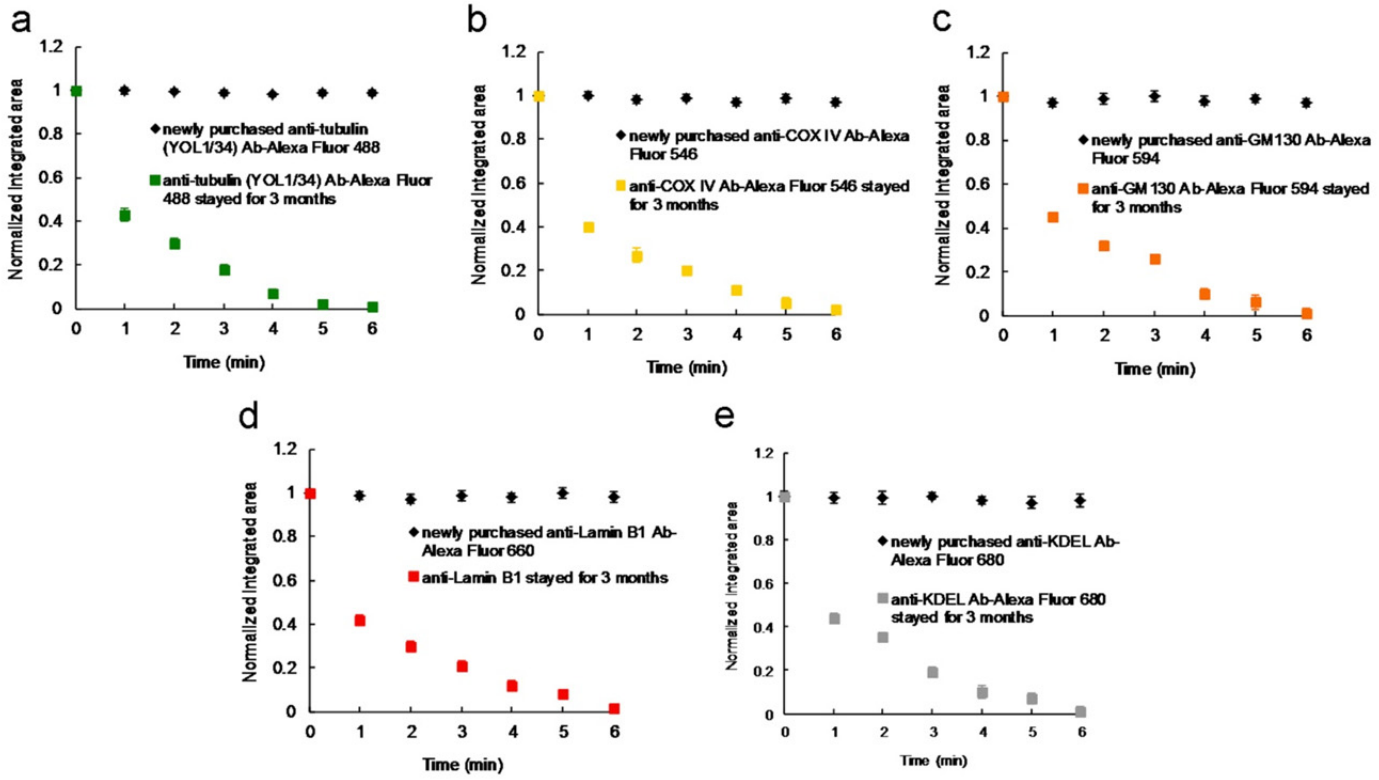

Figure S23. Photostability of (a) $Ab_{microtubule}$ (tubulin, YOL1/34)-Alexa Fluor 488 (abcam, Cambridge, UK), (b) $Ab_{mitochrodrion}$ (COX IV)-Alexa Fluor 546 (abcam, Cambridge, UK), (c) Ab_{golgi} (GM130)-Alexa Fluor 594 (abcam, Cambridge, UK), (d) $Ab_{nucleus}$ $Ab_{nucleus}$ (Lamin B1)-Alexa Fluor 660 (abcam, Cambridge, UK), and (e) Ab_{ER} (KDEL)-Alexa Fluor 680 (abcam, Cambridge, UK), which were subjected to TPE at 14.7 nJ pixel^{-1} for 6 min (approximately 79470 scans). Other emission intensities of integrated area after photoexcitation were respectively divided into that of newly purchased commercially conventional fluorophores (Ab-Alexa Fluor dyes) without photoexcitation, leading to obtain the normalized integrated area. Ex: 800 nm. Delivered dose of material: 0.25 μg mL^{-1}. Data shown are means ± SD (n = 6).

Table S8. TPE action cross sections of fluorescein (in ddH_2O, pH 11) and rhodamine B (in methanol). The TPE wavelength is 800 nm.

	Fluorescein (in ddH_2O, pH=11)	Rhodamine B (in methanol)
Excitation wavelength at 800 nm action cross section, $\eta\ \sigma_2$ (GM, $10^{-50}cm^4s$/photon)	37.5	158.3

Reference

1. Hummers, W. S.; Offeman, R. E. Preparation of Graphitic Oxide. *J. Am. Chem. Soc.* **1958**, *80*, 1339−1339.

2. Rizvi, A. H.; Camara, P. G.; Kandror, E. K.; Roberts, T. J.; Schieren, I.; Maniatis, T.; Rabadan, R. Single-Cell Topological RNA-Seq Analysis Reveals Insights into Cellular Differentiation and Development. *Nat. Biotechnol.* **2017**, *35*, 551−560.

3. Ning, X.; Guo, J.; Wolfert, M. A.; Boons, G. J. Visualizing Metabolically Labeled Glycoconjugates of Living Cells by Copper-Free and Fast Huisgen Cycloadditions. *Angew. Chem. Int. Ed.* **2008**, *47*, 2253−2255.

4. Kuo, W. S.; Chang, C. N.; Chang, Y. T.; Yeh, C. S. Antimicrobial Gold Nanorods with Dual-Modality Photodynamic Inactivation and Hyperthermia. *Chem. Commun.* **2009**, 4835−4837.

5. Kuo, W. S.; Chang, C. N.; Chang, Y. T.; Yang, M. H.; Chien, Y. H.; Chen, S. J.; Yeh, C. S. Gold Nanorods in Photodynamic Therapy, as Hyperthermia Agents, and in Near-Infrared Optical Imaging. *Angew. Chem. Int. Ed.* **2010**, *49*, 2711−2715.

6. Togashi, D. M.; Szczupak, B.; Ryder, A. G.; Calvet, A.; O'Loughlin, M. Investigating Tryptophan Quenching of Fluorescein Fluorescence under Protolytic Equilibrium. *J. Phys. Chem. A* **2009**, *113*, 2757−2767.

7. Sjöback, R.; Nygren, J; Kubista, M. Absorption and Fluorescence Properties of Fluorescein. *Spectrochimica Acta Part A* **1995**, *51*, L7−L21.

8. Kuo, W. S.; Chang, C. Y.; Chen, H. H.; Hsu, C. L. L.; Wang, J. Y.; Kao, H. F.; Chou, L. C. S.; Chen, Y. C.; Chen, S. J.; Chang, W. T.; Tseng, S. W.; Wu, P. C.; Pu, Y. C. Two-Photon Photoexcited Photodynamic Therapy and Contrast Agent with Antimicrobial Graphene Quantum Dots. *ACS Appl. Mater. Interfaces* **2016**, *8*, 30467–30474.

9. Kuo, W. S.; Hsu, C. L. L.; Chang, C. Y.; Kao, H. F.; Chou, L. C. S.; Chen, Y. C.; Chen, S. J.; Chang, W. T.; Tseng, S. W.; Wang, J. Y.; Pu, Y. C. Graphene Quantum Dots Conjugated with Polymers for Two-Photon Properties under Two-Photon Excitation. *Nanoscale* **2016**, *6*, 16874−16880.

10. Cheng, L. C.; Horton, N. G.; Wang, K.; Chen, S. J.; Xu, C. Measurement of Multiphoton Action Cross Sections for Multiphoton Microscopy. *Biomed. Opt. Express* **2014**, *5*, 3427–3433.

11. Weber, G.; Tesla, F. W. Determination of the Absolute Quantum Yield of Fluorescent Solutions. *Trans. Faraday Soc.* **1957**, *53*, 646–655.

12. Velapoldi, R. A.; Tønnesen, H. H. Yields for a Series of Fluorescenct Compounds in the Visible Spectral Region. *J. Fluoresc.* **2004**, *14*, 465–472.

13. Xu, C.; Zipfel, W.; Shear, J. B.; Williams, R. M.; Webb, W. W. Multiphoton Fluorescence Excitation: New Spectral Windows for Biological Nonlinear Microscopy. *Proc. Natl. Acad. Sci. USA* **1996**, *93*, 10763−10768.

14. Lakowicz, J. R. *Principles of Fluorescence Spectroscopy.* 3rd ed.; Springer US: Baltimore, **2006**; pp 1−26.

15. Suhling, K.; Hirvonen, L. M.; Levitt, J. A.; Chung, P. H.; Tregido, C.; Le Marois, A.; Rusakov, D. A.;

Zheng, K.; Ameer-Beg, S.; Poland, S.; Coelho, S.; Henderson, R.; Krstajic, N. Fluorescence Lifetime Imaging (FLIM): Basic Concepts and Recent Developments. *Medical Photonics* **2015**, *27*, 3–40.
16. Kinen, M. M.; Kamal-Eldin, A.; Lampi, A.-M.; Hopia, A. Effect of α- and γ- Tocopherols on Formation of Hydroperoxides and Two Decomposition Products from Methyl Linoleate. *J. Am. Oil Chem. Soc.* **2000,** *77*, 801-806.
17. Sharma, P.; Jha, A. B.; Dubey, R. S.; Pessarakli, M. Reactive Oxygen Species, Oxidative Damage, and Antioxidative Defense Mechanism in Plants under Stressful Conditions. *J. Bot.* **2012**, *2012*, 1–26.
18. Wu, P. C.; Chen, H. H.; Chen, S. Y.; Wang, W. L.; Yang, K. L.; Huang, C. H.; Kao, H. F.; Chang, J. C.; Hsu, C. L. L.; Wang, J. W.; Chou, T. M.; Kuo, W. S. Graphene Oxide Conjugated with Polymers: A Study of Culture Condition to Determine Whether a Bacterial Growth Stimulant or an Anmimicrobial Agent? *J. Nanobiotechnol.* **2018**, *1*6, 1; doi.org/10.1186/s12951-017-0328-8
19. Thompson, A.; Lever, J. R.; Canella, K. A.; Miura, A. Posner, G. H.; Seliger, H. H. Chemiluminescence Mechanism and Quantum Yield of Synthetic Vinylpyrene Analogs of Benzo[a]pyrene-7,8-Dihydrodiol. *J. Am. Chem. Soc.* **1986**, *108*, 4498–4504.
20. Kuo, W. S.; Shao, Y. T.; Huang, K. S.; Chou, T. M.; Yang, C. H. Antimicrobial Amino-Functionalied Nitrogen-Doped Graphene Quantum Dots for Eliminating Multidrug-Resistant Species in Dual-Modality Photodynamic Therapy and Bioimaging under Two-Photon Excitation. *ACS Appl. Mater. Interfaces* **2018**, *10*, 14438–14446.
21. Liu, S.; Zeng, T. H.; Hofmann, M.; Burcombe, E.; Wei, J.; Jiang, R.; Kong, J.; Chen, Y. Antibacterial Activity of Graphite, Graphite Oxide, Graphene Oxide, and Reduced Graphene Oxide: Mechanism and Oxidative Stress. *ACS Nano* **2011**, *5*, 6971–6980.
22. Park, S.; Mohanty, N.; Suk, J. W.; Nagaraja, A.; Piner, J. Q. R. D.; Cai, W.;Dreyer, D. R.; Berry, V.; Ruoff, R. S. Biocompatible, Robust Free-Standing Paper Composed of a TWEEN/Graphene Composite. *Adv. Mater.* **2010**, *22*, 1736–1740.
23. Carmel-Hare, O.; Storz, G. Roles of the Glutathione- and Thioredoxin-Dependent Reduction Systems in the *Escherichia coli* and *Saccaromyces cerevisiae* Responses to Oxidative Stress. *Annu. Rev. Microbiol.* **2000**, *54*, 439–461.
24. Ellman, G. L. Tissue Sulfhydryl Groups. *Arch. Biochem. Biophys*. **1959**, *82*, 70−77.
25. Kuo, W. S.; Chen, H. H.; Chen, S. Y.; Chang, C. Y.; Chen, P. C.; Hou, Y. I.; Shao, Y. T.; Kao, H. F.; Hsu, C. L. L.; Chen, Y. C.; Chen, S. J.; Wu, S. R.; Wang, J. W. Graphene Quantum Dots with Nitrogen-Doped Content Dependence for Highly Efficient Dual-Modality Photodynamic Antimicrobial Therapy and Bioimaging. *Biomaterials* **2017**, *120*, 185−194.
26. Pimenta, M. A; Dresselhaus, G.; Dresselhaus, M. S.; Cancado, L. G.; Jorio, A.; Saito, R. Studying Disorder in Graphite-Based Systems by Raman Spectroscopy. *Phys. Chem. Chem. Phys.* **2007**, *9*, 1276−1290.
27. Ferrari, A. C.; Robertson, J. Interpretation of Raman Spectra of Disordered and Amorphous Carbon. *Phys. Rev. B* **2000**, *61,* 14095−14107.
28. Santana, J. A. C. *Quantitative Core Level Photoelectron Sepctroscopy.* Morgan & Claypool publication:

San Rafael, **2015**; pp 2-1−2-19.
29. Gaspar, D. L.; Polikarpov, E. *OLED Fundamentals: Materials, Devices, and Processing of Organic Light-Emitting Diodes.* CRC Press: Cleveland, **2015**; pp 95−126.
30. Yeh, T. F.; Huang, W. L.; Chung, C. J.; Chiang, I. T.; Chen, L. C.; Chang, H. Y.; Su, W. C.; Cheng, C.; Chen, S. J.; Teng, H. Elucidating Quantum Confinement in Graphene Oxide Dots Based On Excitation-Wavelength-Independent Photoluminescence. *J. Phys. Chem. Lett.* **2016**, *7*, 2087−2092.
31. Rao, A. M.; Eklund, P. C.; Banbow, S.; Thess, A.; Smalley, R. E. Evidence for Charge Transfer in Doped Carbon Nanotube Bundles from Raman Scattering. *Nature* **1997**, *388*, 257−259.
32. Possel, H.; Noack, H.; Augustin, W.; Keilhoff, G.; Wolf, G. An Oxidant, *tert*-Butyl Hydroperoxide (TBHP), to Serve as a Positive Control. *FEBS Lett.* **1997**, *416*, 175−178.